Contents lists available at ScienceDirect

Remote Sensing of Environment

journal homepage: www.elsevier.com/locate/rse

Earth's record-high greenness and its attributions in 2020

Yulong Zhang [a,b,c,*], Jiafu Mao [c,*], Ge Sun [a,*], Qinfeng Guo [a], Jeffrey Atkins [d], Wenhong Li [b], Mingzhou Jin [e], Conghe Song [f], Jingfeng Xiao [g], Taehee Hwang [h], Tong Qiu [i], Lin Meng [j], Daniel M. Ricciuto [c], Xiaoying Shi [c], Xing Li [k], Peter Thornton [c], Forrest Hoffman [c,l]

[a] Eastern Forest Environmental Threat Assessment Center, Southern Research Station, USDA Forest Service, Research Triangle Park, NC, USA
[b] Division of Earth and Climate Sciences, Nicholas School of the Environment, Duke University, Durham, NC, USA
[c] Environmental Sciences Division and Climate Change Science Institute, Oak Ridge National Laboratory, Oak Ridge, TN, USA
[d] USDA Forest Service, Southern Research Station, New Ellenton, SC, USA
[e] Institute for a Secure & Sustainable Environment, University of Tennessee at Knoxville, Knoxville, TN, USA
[f] Department of Geography, University of North Carolina at Chapel Hill, Chapel Hill, NC, USA
[g] Earth Systems Research Center, Institute for the Study of Earth, Oceans, and Space, University of New Hampshire, Durham, NH, USA
[h] Department of Geography, Indiana University Bloomington, Bloomington, IN, USA
[i] Division of Environmental Natural Sciences, Nicholas School of the Environment, Duke University, Durham, NC, USA
[j] Department of Earth and Environmental Sciences, Vanderbilt University, Nashville, USA
[k] School of Geography and Planning, Sun Yat-sen University, Guangzhou, China
[l] Computational Sciences and Engineering Division and Climate Change Science Institute, Oak Ridge National Laboratory, Oak Ridge, TN, USA

ARTICLE INFO

ABSTRACT

Terrestrial vegetation is a crucial component of Earth's biosphere, regulating global carbon and water cycles and contributing to human welfare. Despite an overall greening trend, terrestrial vegetation exhibits a significant inter-annual variability. The mechanisms driving this variability, particularly those related to climatic and anthropogenic factors, remain poorly understood, which hampers our ability to project the long-term sustainability of ecosystem services. Here, by leveraging diverse remote sensing measurements, we pinpointed 2020 as a historic landmark, registering as the greenest year in modern satellite records from 2001 to 2020. Using ensemble machine learning and Earth system models, we found this exceptional greening primarily stemmed from consistent growth in boreal and temperate vegetation, attributed to rising CO_2 levels, climate warming, and reforestation efforts, alongside a transient tropical green-up linked to the enhanced rainfall. Contrary to expectations, the COVID-19 pandemic lockdowns had a limited impact on this global greening anomaly. Our findings highlight the resilience and dynamic nature of global vegetation in response to diverse climatic and anthropogenic influences, offering valuable insights for optimizing ecosystem management and informing climate mitigation strategies.

1. Introduction

Terrestrial vegetation stands as a fundamental constituent of the biosphere, primarily regulating global carbon and water cycles (Gentine et al., 2019), maintaining surface energy balance (Forzieri et al., 2020), and forging interconnections with Earth's climate (Green et al., 2017). Via photosynthesis, global vegetation absorbs CO_2 from the atmosphere, transforming it into vital carbohydrate resources (Beer et al., 2010). These resources, in turn, underpin the food web chain (Pimm et al., 1991), define planetary boundary (Running, 2012), and offer numerous ecosystem services such as wood production, providing clear water, and serving as a natural solution for offsetting anthropogenic carbon

emissions (Griscom et al., 2017). Therefore, systematically monitoring and assessing global vegetation status is imperative to understand Earth system processes (Falkowski et al., 2000), develop strategies for climate mitigation and adaptation (Canadell and Raupach, 2008), and support ecosystem management and human welfare (Imhoff et al., 2004).

While satellite observations since 1982 have highlighted augmented vegetation activity over terrestrial landscapes (Zhu et al., 2016), this greening trend demonstrates considerable variability across various time periods, biomes and climate zones (Mao et al., 2016; Zhang et al., 2017b; Chen et al., 2019; Piao et al., 2020). This verdant expansion, particularly evident within natural vegetation, has shown signs of deceleration (Pan et al., 2018; Winkler et al., 2021), attributed to

---

* Corresponding authors.
  E-mail addresses: yulong.zhang@duke.edu (Y. Zhang), maoj@ornl.gov (J. Mao), ge.sun@usda.gov (G. Sun).

climate-related negative feedback loops (Liu et al., 2023a, 2023b) and human disturbances (Matricardi et al., 2020; Liu et al., 2023a, 2023b). According to NASA records (NASA, 2024), global climate has warmed by 1.3 degrees Celsius since 1880, with the ten warmest years on record occurring in the last two decades. Regions constrained by low temperatures, such as boreal and alpine domains, could benefit from this warming climate (Keenan and Riley, 2018), while other regions, especially humid and semi-arid zones, might confront a subdued vegetation vigor from heat and drought stresses (Vicente-Serrano et al., 2013). In addition, human activities such as deforestation and urbanization have significantly altered ecosystem structures and functions (Zhang et al., 2021). To date, a thorough assessment of the global vegetation status and its driving factors, especially within the context of multi-year trends and variability, remains incomplete.

The pandemic from the coronavirus disease 2019 (COVID-19) has cast a grave shadow over public health and global economic prosperity (Ciotti et al., 2020). As a secondary effect, the extensive lockdowns, travel restrictions, and reduced energy consumption during the pandemic (Onyeaka et al., 2021), have resulted in the most substantial short-term decline in global CO_2 emissions since 1960 (Liu et al., 2022), and spawned a beneficial side effect of improved air quality (Venter et al., 2020), which could in turn promote vegetation growth by enhancing radiation levels (Su et al., 2021; Liu et al., 2024b). Nonetheless, the situation is complicated by secondary climate effects caused by the pandemic-induced alterations in atmospheric constituents such as aerosols and ozone (Lamboll et al., 2021). In addition, regional climate variability such as precipitation and temperature anomalies, driven by climate oscillations like La Nina and Indian Ocean Dipole, could potentially counteract or modulate these COVID-19-associated effects (Weir et al., 2021). Currently, a detailed evaluation of the impact of COVID-19 on global vegetation anomalies has yet to be conducted.

Here, we explored the global vegetation status since 2001 with a focus on the pandemic year of 2020 from a diverse range of remote sensing datasets. Moreover, we investigated the drivers behind both accumulated trend-related and instantaneous variation-related anomalies in global vegetation activity based on the ensemble machine learning (Caruana et al., 2004; Zhang et al., 2023) and land surface model simulations from Trends in Net Land-Atmosphere Carbon Exchange Determined by Yields (TRENDY) (Sitch et al., 2015). The potential vegetation impacts from COVID-19 were also examined using the Earth system model simulations from the COVID-19 Model Intercomparison Project (COVID-MIP) (Lamboll et al., 2021). Despite the transient reduction in carbon emissions resulting from COVID-19 may not be commensurate with the scale of the ongoing record levels of greenhouse gas emissions, this unprecedented disruption may present a unique opportunity to explore the response and feedback of the Earth system to human activities (Diffenbaugh et al., 2020). Thus, a thorough comprehension of the global vegetation status in 2020 provided by this study holds the potential to yield valuable insights into the nuanced disruptions of the carbon cycle linked to anthropogenic interventions.

2. Materials and methods

2.1. Multi-source remote sensing data

To evaluate global greening status, we utilized three groups of remote sensing-based vegetation indices (VI), including Enhanced Vegetation Index (EVI), Solar-induced Fluorescence (SIF) and leaf area index (LAI). EVI is designed to enhance vegetation signals in high biomass regions while reduce soil and atmospheric background influences (Huete et al., 2002), making it especially effective in areas where traditional indices like normalized difference vegetation index may saturate and fail to capture variability. SIF serves as a direct, real-time indicator of plant health and stress by measuring the chlorophyll fluorescence in the red and far-red spectrum emitted during photosynthesis (Krause and Weis, 1991). LAI is a measure of canopy density

defined as the total leaf area per unit ground surface area (Fang et al., 2019), which is closely associated with vegetation activity and productivity. Overall, EVI and LAI are more about the structure and density of vegetation (Fang et al., 2019), while SIF reflects the physiological and functional attributes of plants (Sun et al., 2023). Here we used them in conjunction to provide a more comprehensive characterization of global vegetation status and dynamics.

We adopted three global monthly 0.05° EVI products, including MODIS EVI from Terra (MOD13C2) for 2001–2020 and Aqua (MYD13C2) satellites for 2003–2020 in the C6.1 version, along with VIIRS EVI from the Suomi NPP satellite (VNP13C2) covering 2012–2020. In addition, we derived a global monthly 0.05-degree EVI dataset (referred to as MCD43-EVI) from global daily seamless land surface reflectance product (Liang et al., 2024). This reflectance dataset underwent multiple processing steps, including Bidirectional Reflectance Distribution Function (BRDF) correction (using MOD09GA/MYD09A1 and MCD43A3 NBAR), outlier detection, gap filling, and smoothing to address low-quality conditions such as cloud contamination (Liang et al., 2024).

We used three global 0.05° SIF products: 8-day reconstructed TROPOMI SIF (RT-SIF) (Chen et al., 2022a) from 2001 to 2020, monthly Global OCO-2 based SIF (GO-SIF) (Li and Xiao, 2019) for the same period, and the 16-day Global Contiguous SIF (GC-SIF) (Yu et al., 2019b) from 2015 to 2020. Note that global SIF products selected here are not direct observations, but retrieved products based on original SIF measurement and supplemented by a series of remote sensing and geophysical data. For example, RTSIF is a reconstructed global SIF product based on the original TROPOMI SIF and by incorporating a series of remote sensing indicators including the gap-filled MODIS BRDF product, MODIS land surface temperature and CERES photosynthetic active ration (Chen et al., 2022a, 2022b).

We further included three global LAI products in our study: the monthly reprocessed 0.05° MODIS C6 LAI (Yuan et al., 2011; Yan et al., 2016) from 2003 to 2020, biweekly 1/12° GIMMS4g V1.2 LAI (Cao et al., 2023) and 8-day 0.073° GLOBMAP V3 LAI (Liu et al., 2012; Chen et al., 2020) from 2001 to 2020. All the global VI products have been gap-filled by the producers using different strategies to minimize the effects of cloud contamination and other issues. As a result, these products are continuous and consistent in space and time, making them ready for global analysis. In this study, these 8-day or monthly VI products with negative values treated as zero were averaged to annual values for further analysis. Global land cover data from MODIS (MCD12C1 C6.1) (Sulla-Menashe et al., 2019) was used to mask out unvegetated areas based on the majority rule in the classification scheme of the International Geosphere-Biosphere Programme (IGBP) during 2001 to 2020. All sources of remote sensing products used in this study were seen in Table S1.

We opted not to define a specific growing season in our study, owing to the non-uniform thresholds of different indicators and the lack of meaningful interpretation when computing a global mean from pixel-level averages of the growing season (Zhang et al., 2017a, 2017b; Chen et al., 2019). Nevertheless, we conducted a validation test using a simplified growing season (GS) definition, where monthly air temperature exceeds 0 °C and the specific VI is above a conservative threshold (0.05 for EVI and 0.01 for LAI and SIF). Such a GS definition is dynamic and can minimize the snow and ice effects in the non-growing season. We then calculated the annual GS length and GS accumulated total VI for each indicator on the global scale (Fig. S1). Notably, our analysis revealed that the GS total value closely aligns with the annual mean value at the global scale among different VIs (Fig. S1), supporting the validity of using annual mean values for our global analysis.

2.2. Decomposition of annual anomaly signal

To better understand global greening status in 2020, we decomposed the annual greenness anomaly to the long-term trend-related and short-

term variation-related components both at the global scale (Fig. 1) and the pixel scale. We first normalized the annual long-term series of greenness as Z-scores:

$$Z = (G - \mu)/\sigma \tag{1}$$

where Z represents Z-score; G denotes the annual greenness, measured in terms of EVI, SIF and LAI; μ and σ are multi-year mean and standard deviation of G, respectively, calculated over the overlapping period from 2003 to 2020.

Utilizing the normalized greenness, we then derived the trend-related (G_t) and variation-related (G_v) anomalies through a least-squares linear regression model:

$$Z_t = \beta_0 + \beta_1 \times T_t + \epsilon_t \tag{2}$$

$$G_t = Z_t - \epsilon_t \tag{3}$$

$$G_v = \epsilon_t \tag{4}$$

where Z_t is the annual normalized greenness for year t; β_0 is the intercept of the regression; β_1 is the slope coefficient, indicating the greening rate during the study period; T_t is the time variable (year) for the calculated anomaly; and ϵ_t represents the regression residual, accounting for the variation in the annual anomaly signal that is not explained by the time trend. This straightforward method could help us to effectively isolate the trend-related component (G_t) from the variation-related component (G_v) within the total greenness anomaly (Z_t), offering a clearer perspective on the global greening status in a specific year, such as 2020.

2.3. Modeling and attribution of global greening based on the ensemble machine learning

To simulate and attribute global greening in 2020, we developed a global greenness model using the ensemble machine learning (EML). As a meta-approach in machine learning, EML could boost accuracy, robustness, and effectiveness by integrating predictions from multiple ML models (Caruana et al., 2004; Sagi and Rokach, 2018). Here, our ensemble included five state-of-the-art MLs: Random Forest, CatBoost, XgBoost, LightGBM and Multi-Layer Perceptron (Zhang et al., 2023). Random Forest employs a bagging approach, aggregating multiple decision trees for stronger predictions (Breiman, 2001). CatBoost, XgBoost, and LightGBM adopt the strategy of gradient boosting to build decision trees sequentially, each differing in specific algorithmic nuances (Chen and Guestrin, 2016; Ke et al., 2017; Prokhorenkova et al., 2018). As a deep learning approach, the Multi-Layer Perceptron consists of multiple layers of neurons inspired by biological neural networks and uses backpropagation and gradient-based optimization methods to update weights (Abiodun et al., 2018). Collectively, the chosen ML models, distinct in their structure and parameters, are anticipated to provide extensive capabilities in capturing the complex interactions between global vegetation dynamics and their underlying drivers.

To construct our EML model, we incorporated several key factors related to climate variability (solar radiation, air temperature, precipitation), land cover change (proportions of croplands and forests), CO_2 concentration, and nitrogen deposition as inputs, in alignment with previous studies (Huang et al., 2018) and the TRENDY project (Sitch et al., 2015). The climate data were sourced from TerraClimate (Abatzoglou et al., 2018), while the annual land cover dynamics was extracted from the MODIS product (MCD12C1 C61). Annual CO_2 records and nitrogen deposition (a sum of dry and wet depositions) were adopted from the inputs used in TRENDY (Sitch et al., 2015). The output or prediction of the model was annual LAI from MODIS. To compare with TRENDY, we set the model's spatial resolution as 0.5 degree.

For the training process, we randomly selected 80 % of the global total vegetated pixels for training ($\sim$ 0.73 million records) and the remaining 20 % for validation ($\sim$ 0.18 million records). Throughout this process, we fine-tuned each ML model and their ensemble using five-fold cross-validation. Specifically, optimization of each ML model was executed utilizing the grid search algorithm, following which an ensemble output was derived by integrating the predictions from these models with assigned weights:

$$\widehat{G} = \sum_{i=1}^{N} \left(w_i \bullet G_{i,x} \right) \tag{5}$$

where $\widehat{G}$ denotes the estimated ensemble output for greenness; N is the number of the total involved ML models in this study, constrained to a maximum of five; $G_{i,x}$ is the prediction of the ith ML model given an input of x; and w_i is the weight assigned to the prediction of the ith model. The optimization of these weights was achieved through an approach named forward stepwise ensemble selection (Caruana et al., 2004) by minimizing the root mean square error (RMSE) between the prediction and observation for all training samples. Unlike the simple averaging method that assigns uniform weights across all base models, our selected approach is underpinned by a greedy search-based algorithm, renowned for its efficiency and robustness, particularly in mitigating overfitting issue (Caruana et al., 2004). The framework of EML has been approved to effectively simulate global fire dynamics (Zhang et al., 2023).

We executed the optimization and evaluation of EML based on the open accessed Automated Machine Learning Python package of mljar (Version 1.1.2; https://github.com/mljar/mljar-supervised). The optimized parameters for the five involved machine learning models were presented in Table S2. Performance evaluation revealed that LightGBM achieved the best results with the lowest RMSE, followed by XgBoost, Random Forest, CatBoost and Neural Network (Fig. S2). Based on the forward stepwise ensemble selection mentioned above, we identified LightGBM and XbBoost as the best combination to construct the final ensemble with their weight as 0.6 and 0.4, respectively. Utilizing global
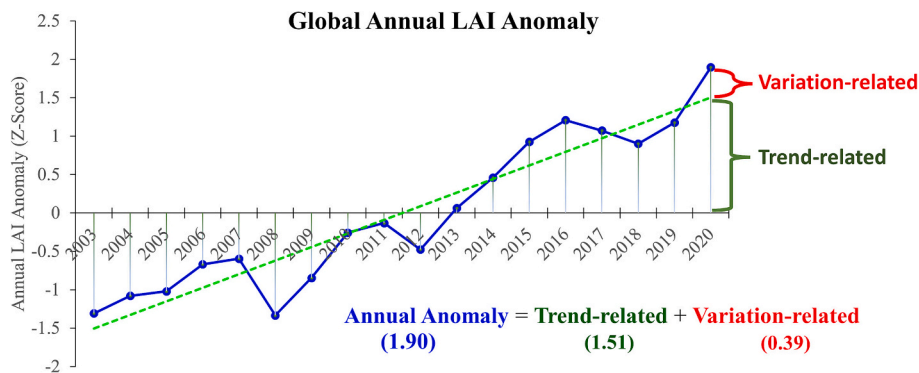

Fig. 1. Example of the decomposition of global greenness anomaly in 2020 into the trend-related and variation-related components. The data here is global annual mean LAI from MODIS. Annual data is normalized to the Z-score based on its multi-year mean and standard deviation from 2003 to 2020.

Table 1
Scenario design to delineate vegetation controls linked to climate change, land use/cover change (LUCC), rising CO_2 and nitrogen deposition. The symbol '+' indicates that an input variable varies over time, while the symbol '-' indicates that the variable remains fixed at its initial 2003 level. The impact of specific factors or factor groups on vegetation is assessed by the difference between the 'All' scenario and each individual scenario.

Simulations	Climate			LUCC	CO_2	Ndep
	RAD	TMP	PRE			
All	+	+	+	+	+	+
RAD_control	−	+	+	+	+	+
TMP_control	+	−	+	+	+	+
PRE_control	+	+	−	+	+	+
CLM_control	−	−	−	+	+	+
LUCC_control	+	+	+	−	+	+
CO2_control	+	+	+	+	−	+
Ndep_control	+	+	+	+	+	−

validation data excluded from the training phase (20 %), we found the optimized EML accurately predicted annual LAI with non-systematic errors (slope = 1.01), achieving an RMSE of 0.2 m^2 m^{-2}. This outcome markedly exceeds the performance of the TRENDY LAI (shown in the next section), which recorded a slope of 1.21 and an RMSE of 1.23 m^2 m^{-2} (Fig. S3). Spatially, EML was approved to better simulate the annual total anomaly of LAI and their trend-related and variation-related components in 2020 compared to TRENDY (Fig. S4; Table S3). Nonetheless, both EML and TRENDY showed limitations in capturing subtle anomaly signals when compared to the annual absolute values. A similar limitation has been noted in ML-based global carbon and water flux datasets (Tramontana et al., 2016).

Leveraging the optimized EML along with global model inputs, we systematically quantified the controls on vegetation greenness related to climate change, land use/cover change (LUCC), rising CO_2 and nitrogen deposition through factorial simulation running (Table 1). Initially, a comprehensive simulation was conducted where all group factors were allowed to vary over time (2003−2020), designated as "All". Subsequent simulations involved maintaining one factor group at its 2003 baseline level, while permitting variations in the other groups over time. The influence exerted by each individual factor group was then deduced by calculating the differences between the 'All' scenario and these individual simulations (Table 1).

To identify the spatial pattern of major controls on the trend-related anomaly in 2020, we compared annual trends of simulated LAI from 2003 to 2020 across four impact groups: climate change, LUCC, rising CO_2 and nitrogen deposition. We used the non-parametric Theil-Sen estimator to calculate these trends, noting its effectiveness in handling outliers (Fernandes and Leblanc, 2005). The factor group exhibiting the highest absolute trend, either positive or negative, was labeled as the "major control", and its global impact area was subsequently quantified. For the variation-related greenness anomaly in 2020, we identified its primary climate control by comparing the de-trended LAI simulated from solar radiation (RAD), air temperature (TMP) and precipitation (PRE). Six primary climate controls were identified based on their respective impacts, categorized as either positive or negative: positive radiation controls (RAD+), negative radiation controls (RAD-), positive temperature controls (TMP+), negative temperature controls (TMP-), positive precipitation controls (PRE+), and negative precipitation controls (PRE-).

2.4. Comparison of vegetation controls between EML and TRENDY

TRENDY is a collaborative scientific project that integrates a suite of process-based land surface models known as Dynamic Global Vegetation Models (DGVMs) to understand and quantify global carbon cycle's drivers and processes (Sitch et al., 2015; Friedlingstein et al., 2022). These models, noted for their structural complexity, incorporate

physiological and biogeochemical processes, offering a process-based perspective on global vegetation dynamics (Zhu et al., 2016; Piao et al., 2020). This contrasts with machine learning models that are primarily driven by data and statistical approaches and lack of explainability as a "black box" (Roscher et al., 2020). However, TRENDY encounters challenges such as dependence on model assumptions, uncertainties in structure and parameters, and the quality of input data, along with the complexities arising from their interactions and compensations (Zhou et al., 2018; Bastos et al., 2020; Zhang et al., 2021).

To compare with vegetation controls from EML, we included annual LAI simulations from 17 DGVMs in TRENDY version 10 (Table S4) and calculated their ensemble mean and standard deviation for analysis. Based on the protocol simulations, we derived the land use change effect by calculating the difference between scenarios S3 (CO_2, climate and land use changes) and S2 (CO_2 and climate changes), climate change effect by the difference between S2 and S1 (CO_2 change only), and CO_2 effect by the difference between S1 and S0 (a control scenario with no forcing changes). Since TRENDY models with N cycle have time-varying N inputs for all scenarios, the nitrogen deposition effect cannot be isolated and intertwined with the CO_2 fertilization effect. To directly compare the CO_2 effect derived from EML, we further calculated the ensemble mean of six models from TRENDY with only considering CO_2 fertilization effect (Table S4).

We used TRENDY to quantify controls on the trend-related anomaly in 2020 with a similar approach for EML (see above sections). For the variation-related anomaly, TRENDY did not have specific climatic simulations. Therefore, it is not used to compare with EML. The spatial resolutions of model outputs from TRENDY range from 0.5 to 2 degrees. For consistency with EML, all TRENDY outputs were resampled to a 0.5 degree. We acknowledged that the comparison between TRENDY and EML is not strictly aligned, given the differences among model inputs, scenario designs, and factors considered. For instance, TRENDY utilized global Land Use Harmonization data with a coarse spatial resolution (0.25 degree) with a primary focus on land use change impact (Yu et al., 2019a, 2019b), whereas EML employed MODIS land cover dynamics with moderate resolution (500 m) mainly reflecting land cover change effects, but missing land use information (Zhang et al., 2021). The difference in model configuration between EML and TRENDY may also contribute to discrepancies in their spatial controls. Nonetheless, juxtaposing process-based modeling with machine learning provides valuable insights into global vegetation controls revealed by these distinct modeling strategies.

2.5. Delineating regions impacted by COVID-19 lockdowns

The pandemic prompted widespread lockdowns aimed at curtailing the rapid spread of the coronavirus in 2020 (Diffenbaugh et al., 2020). However, the nature and extent of these lockdowns varied considerably across countries (Liu et al., 2020, 2022), influenced by diverse public health strategies, healthcare capacities, and socio-political contexts (Onyeaka et al., 2021). To gauge the extent of potential vegetation influence from these lockdowns, we calculated the annual anomaly of ground-level NO_2 in 2020 relative to that of 2019. NO_2 is a sensitive indicator of the impact of COVID-19 lockdown because the reduced emissions from the weakened transportation and industrial activities could significantly decrease near-surface concentrations of NO_2 (Venter et al., 2020). Here, global daily 1-km NO_2 concentrations from Sentinel-5P NRTI was adopted to calculate the annual medium values of NO_2 for both 2020 and 2019. To construct the clear-sky data, pixels with cloud fractions larger than 30 % were removed. Following empirical tests, a decline threshold of 0.05 for the total vertical column of NO_2 (defined as the ratio of the slant column density of NO_2 and the total air mass factor) was then applied to delineate areas potentially influenced by COVID-19 lockdowns.
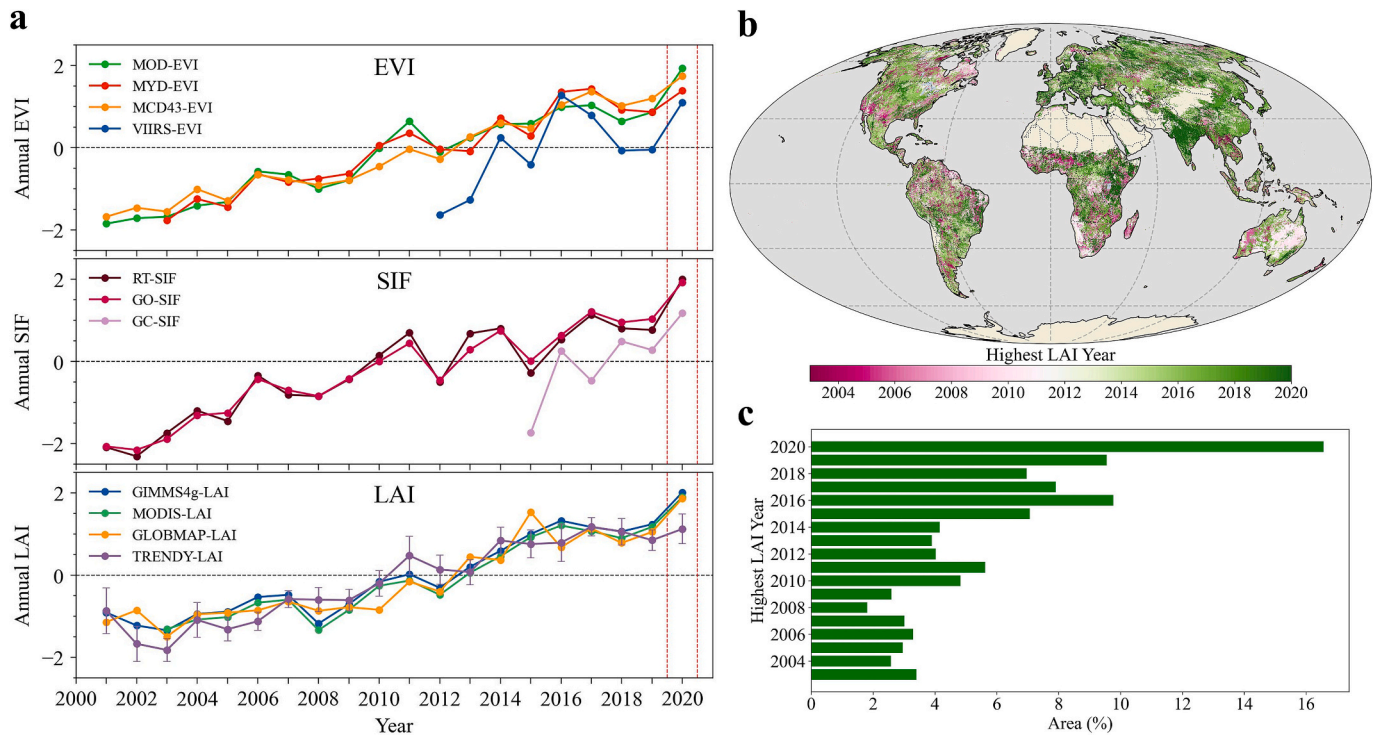
Fig. 2. Interannual change of global vegetation activity from satellite remote sensing observations since 2001. (a) Annual anomalies in global vegetation activity with a focus on the year 2020 (marked by red dashed vertical lines) in terms of Enhanced Vegetation Index (EVI), Sun-Induced Fluorescence (SIF) and Leaf Area Index (LAI). All anomalies are normalized to Z-scores using their multi-year means and standard deviations during the overlapping period of 2003 to 2020. For VIIRS-EVI, the period is from 2012 to 2020, while for GC-SIF, the period is from 2015 to 2020. The error bar in TRENDY-LAI represents one standard deviation from the ensemble models from TRENDY. (b) Spatial pattern of years with the highest LAI values during 2003 to 2020. (c) Fractional areas for the year with the highest LAI. The area is relative to the global total vegetated area. (b) and (c) are based on MODIS LAI. (For interpretation of the references to colour in this figure legend, the reader is referred to the web version of this article.)

2.6. Quantifying COVID-19 effect on global greening anomaly through COVID-MIP

The widespread lockdowns induced by COVID-19 resulted in a notable reduction in greenhouse gas emissions and significantly altered atmospheric constituents like aerosols, ozone, and optical properties (Lamboll et al., 2021). These atmospheric changes are expected to influence the climate, subsequently affecting vegetation growth in both lockdown and unlock down regions. In response to these phenomena, COVID-MIP represents a collective of Earth system models designed to simulate the modified scenarios that reflect the climatic impacts of the COVID-19 pandemic (Lamboll et al., 2021). This initiative aims to understand and quantify the environmental repercussions of the pandemic-related changes on a global scale. Here, we adopted the Max Planck Institute Earth System Model (MPI-ESM1.2) (Mauritsen et al., 2019) from COVID-MIP to evaluate the influence of COVID-19 on global greening due to the availability of LAI simulation (Table S1). Annual simulations for short-term COVID-19 effect from 2020 to 2024 were involved in this study. To control the background climate variations unrelated to the pandemic, baseline simulations running at the SSP2–4.5 scenario from 2015 to 2024 were further obtained. To quantify the uncertainty in both the COVID-MIP and the baseline, ten distinct simulations were employed, each with a unique model initiation, spanning from r1i1p1f99 to r10i1p1f99. Following the simulations, the ensemble mean and standard deviation across these model runs were calculated. The effect of COVID-19 on vegetation greening anomaly both over lockdown and unlock down regions were then evaluated by comparing the difference between COVID-MIP and the baseline running. Note that COVID-MIP only simulated the direct climate forcing effects caused by COVID-19, but not included the anthropogenic-induced land cover changes. Here we used yearly land cover data from MODIS (Table S1) to characterize land cover change and then used EML simulations to quantify its effect on annual LAI anomaly in 2020 over the lockdown region.

2.7. Greening variability across climate zones and their potential linkage with ENSO

Four climate zones including tropical, arid/semi-arid, temperate, and boreal/alpine (Fig. S5) were identified using the 1-km Köppen-Geiger climate classification (Beck et al., 2018). To evaluate the contributions of these climate zones to global greenness variability, annual area-weighted total LAI values were computed for each zone from 2003 to 2020. For each climate zone, the long-term trend was removed, and a Z-score was calculated to identify years with significant anomalies exceeding one standard deviation. We utilized the monthly Oceanic Niño Index (ONI) from National Oceanic and Atmospheric Administration (NOAA) to monitor both moderate (ONI > 1.0) and strong (ONI > 1.5) phases of El Niño and La Niña events[1], which are potentially linked with global and regional greenness variability.

3. Results

3.1. Earth's exceptional greening in 2020

Global vegetation reached its peak greening in 2020, continuing a long-term trend since 2001 (Fig. 2). This is evidenced by three groups of vegetation activity proxies from ten remote sensing-based products, including EVI, SIF and LAI (Fig. 2a). Specifically, annual Z-scores

---

[1] https://ggweather.com/enso/oni.htm.

(defined as the annual anomaly normalized by the standard deviation [σ]) for global averaged EVI, SIF and LAI in 2020 are 1.69 ± 0.23 σ (MOD-EVI, MYD-EVI and MCD43-EVI), 1.97 ± 0.04 σ (RT-SIF and GO-SIF), and 1.92 ± 0.06 σ (MODIS-LAI, GIMMS4g-LAI and GLOBMAP-LAI), respectively. The ensemble land surface models from TRENDY also captured the presence of such a greening peak in 2020, but with a lower amplitude on annual LAI (1.13 ± 0.36 σ) when compared to remote sensing products (1.90 σ for MODIS-LAI, 1.93 σ for GIMMS4g-LAI and 1.87 σ for GLOBMAP-LAI) (Fig. 1a). It is worth noting that MYD-EVI showed a peak greening year in 2017, while VIIRS-EVI indicated 2016 as the peak year, with both products recognizing 2020 as the second-highest greening year. However, when accounting for the growing season, the integrated annual values for both MYD-EVI and VIIRS-EVI were still highest in 2020 (+0.19σ and + 0.88σ higher than in 2017 and 2016, respectively), aligning with the patterns observed in the other eight global VI products (Fig. S1).

Spatially, multi-year peak greenness exhibits a heterogeneous pattern with more recent peak values (towards 2020) predominantly concentrated in India, central Europe, eastern Africa, and parts of China (Fig. 2b). China and India are two leading contributors to global greening (Chen et al., 2019). However, India showed a much higher fraction of multi-year peak greenness (74.1 %) in 2020 compared to China (17.7 %) (Fig. S6). Globally, the year 2020 exhibited the highest fraction of annual peak greenness as measured by MODIS LAI over the vegetated area (18.6 %), much higher than the subsequent years of 2016 (10.6 %) and 2019 (10.3 %) (Fig. 2c). A similar notable peak in 2020 for the multi-year maximum LAI was also reflected by GIMMS4g LAI and GLOBMAP-LAI data (Fig. S7), although subsequent years displayed variability. Since both GLOBMAP-LAI and GIMMS4g-LAI were developed based on MODIS-LAI data, we acknowledge this comparison was somewhat relative.

3.2. The greening anomaly of 2020 contributed by trend-related and variation-related components

To better understand the annual greenness anomaly in 2020, we decomposed it into two distinct components: accumulated trend-related anomaly and instantaneous variation-related anomaly (Fig. 1). Globally, terrestrial vegetation exhibited a significant positive anomaly of 1.90 σ in 2020 relative to the multi-year mean based on MODIS LAI, with a higher contribution from the trend-related anomaly (1.51 σ) than the variation-related anomaly (0.39 σ).

Spatially, the trend-related anomaly showed positive patterns over 76.7 % of total vegetated area, widely spread from major continents except Australia (Fig. 3b). In contrast, the variation-related anomaly showed positive patterns in a lesser extent (53.6 % of total area), mainly concentrating in India, eastern Africa and Brazil, and western Russia (Fig. 3c). Notably, the variation-related anomaly showed nearly double negative areas (46.3 %) than the trend-related area (23.3 %), which were mainly located in Southern China, western Australia, southern Argentina and most North America (Fig. 3c).

When combined, the positive trend-related anomaly was intensified by the positive variation-related anomaly across approximately 41.4 % of the total vegetated area, with a particular concentration in India and central Russia (Fig. 3d). Nevertheless, a contrasting pattern persisted across 35.4 % of the total vegetated region, where the positive trend-related anomaly contends with a counteracting negative variation-related anomaly. This occurrence is predominantly situated in regions like China, a substantial portion of North America, and southern Argentina. Consequently, the leading greening country of China showed a lower anomaly of greenness (i.e., +1.35 σ) than India in 2020 (+2.66 σ; Fig. S8). Notably, a small portion of the vegetated area (11 %), primarily located in Australia and eastern Canada, showed both negative trend- and variation-related anomalies. A comparable extent of regions
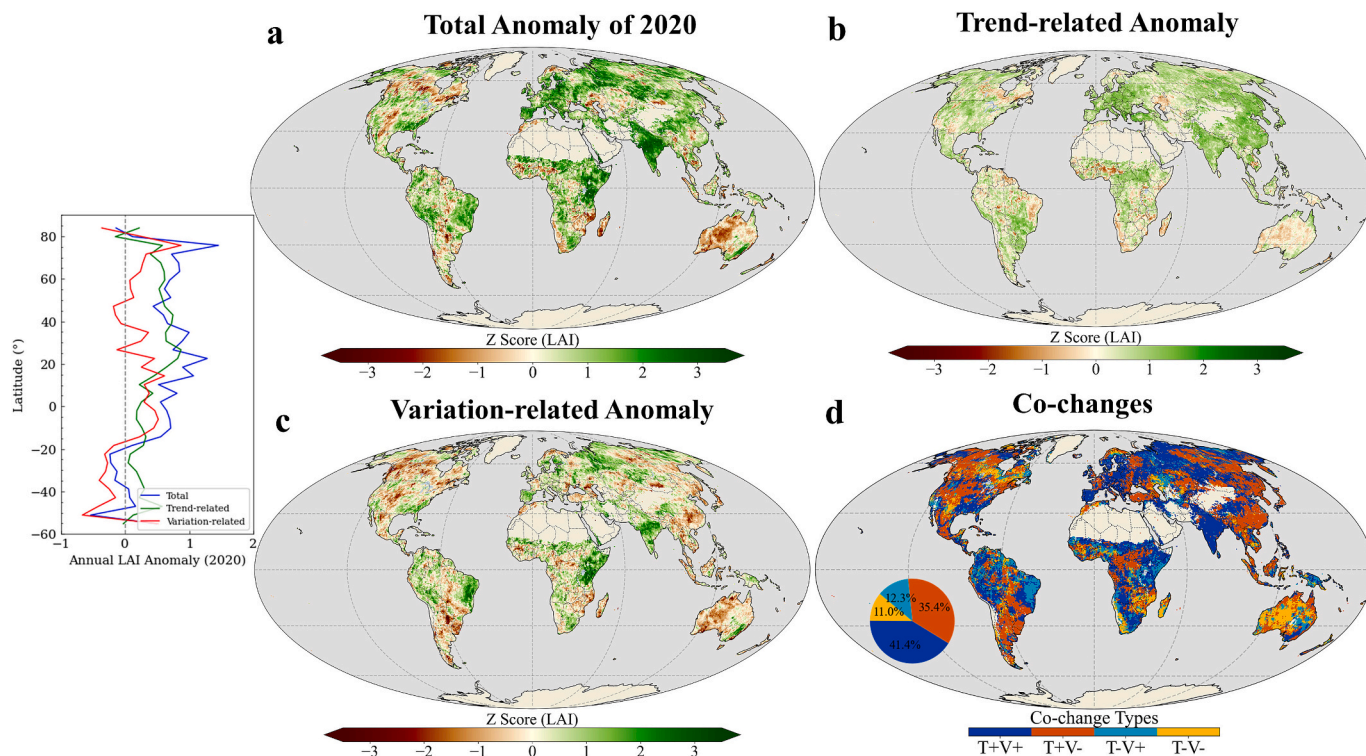

Fig. 3. Spatial patterns of annual greenness anomaly in 2020 contributed by trend-related and variation-related components based on MODIS LAI. (a) Annual total greenness anomaly in 2020. (b) Annual trend-related greenness anomaly in 2020. (c) Annual variation-related greenness anomaly in 2020. (d) Co-changes from trend-related (T) and variation-related (V) components on annual total greenness anomaly; '+' and '-' in the legend indicate positive and negative anomalies, respectively. The insect chart on the left shows latitudinal distributions of annual total anomaly in (a) and its two components (b) & (c). The insect pie chart in (d) shows the relative portion of each category to the global total vegetated area.

(12.3 %) demonstrated the counteraction of the negative trend-related anomaly by the positive variation-related anomaly, which were mostly scattered in tropical regions (Fig. 3d). Two other independent vegetation indicators, SIF and EVI, showed similar patterns of co-changes between trend-related and variation-related anomalies (Fig. S9).

3.3. Attributions of annual trend-related and variation-related anomalies in 2020

Through simulations from the ensemble machine learning (EML) models, we explored primary factors influencing both trend- and variation-related anomalies in global vegetation greenness in 2020 (Fig. 4). We found that the rising atmospheric CO_2 dominated the accumulated trend-related anomaly over 42.4 % of the total vegetated area, followed by climate change (30.4 %), land use/cover change (LUCC) (15.5 %) and nitrogen deposition (11.7 %) (Fig. 4a). Globally, our EML-based approach well simulated the global LAI trend from MODIS with a marginal error of −1.5 %, and the underlying drivers of this trend were generally in alignment with the land surface models from the TRENDY project (Fig. 4b). However, the EML-based models exhibited superior performances in simulating annual LAI trends at the regional scale compared to TRENDY (Figs. S3 & S4). Overall, the EML-based approach revealed a more extensive CO_2 association with the greening trend, especially in arid/semi-arid and temperate zones, as opposed to the tropical emphasis reflected by TRENDY (Fig. S10). In addition, the EML-based approach accentuated the negative effect of

LUCC in tropical regions, yet concurrently underscored the positive impacts of LUCC in temperate regions (such as China), which is not shown in TRENDY (Fig. S11). Notably, the EML approach uncovered a dominant impact of nitrogen deposition in regions with sparse vegetation, such as the Tibetan Plateau and eastern Africa (Fig. 4a), a nuance that is not distinctly delineated by TRENDY.

For the instantaneous variation-related anomaly of LAI in 2020, precipitation showed the major control over 37.4 % of the global vegetated area, which is comparable to the radiation control (36.1 % of the total area), but larger than temperature control (26.4 % of the total area) (Fig. 4c). Spatially, the strong wetting anomaly and the accompanying radiation variation (Fig. S12) were the primary drivers of the observed positive greenness anomaly in regions such as eastern Brazil, eastern Africa, and most of India (Fig. 4c). Additionally, a warming anomaly had contributed to a positive greenness anomaly in northern Eurasian. Conversely, the substantial drying anomaly was responsible for a negative greenness anomaly observed in central Austria and North America. Notably, a dimming condition was associated with a negative greenness anomaly in southern China, whereas a brightening condition was linked to a negative greenness anomaly in southern Argentina (Figs. S12 & 4C).

Among the four climate zones (Fig. S5), the boreal/alpine zone had the highest contribution to the global area-weighted greenness anomaly in 2020, accounting for 31.7 % (Fig. 4d). In contrast, the arid/semi-arid zone had the smallest share at 14 %. The tropical and temperate zones registered intermediate contributions of 30.6 % and 23.7 %,
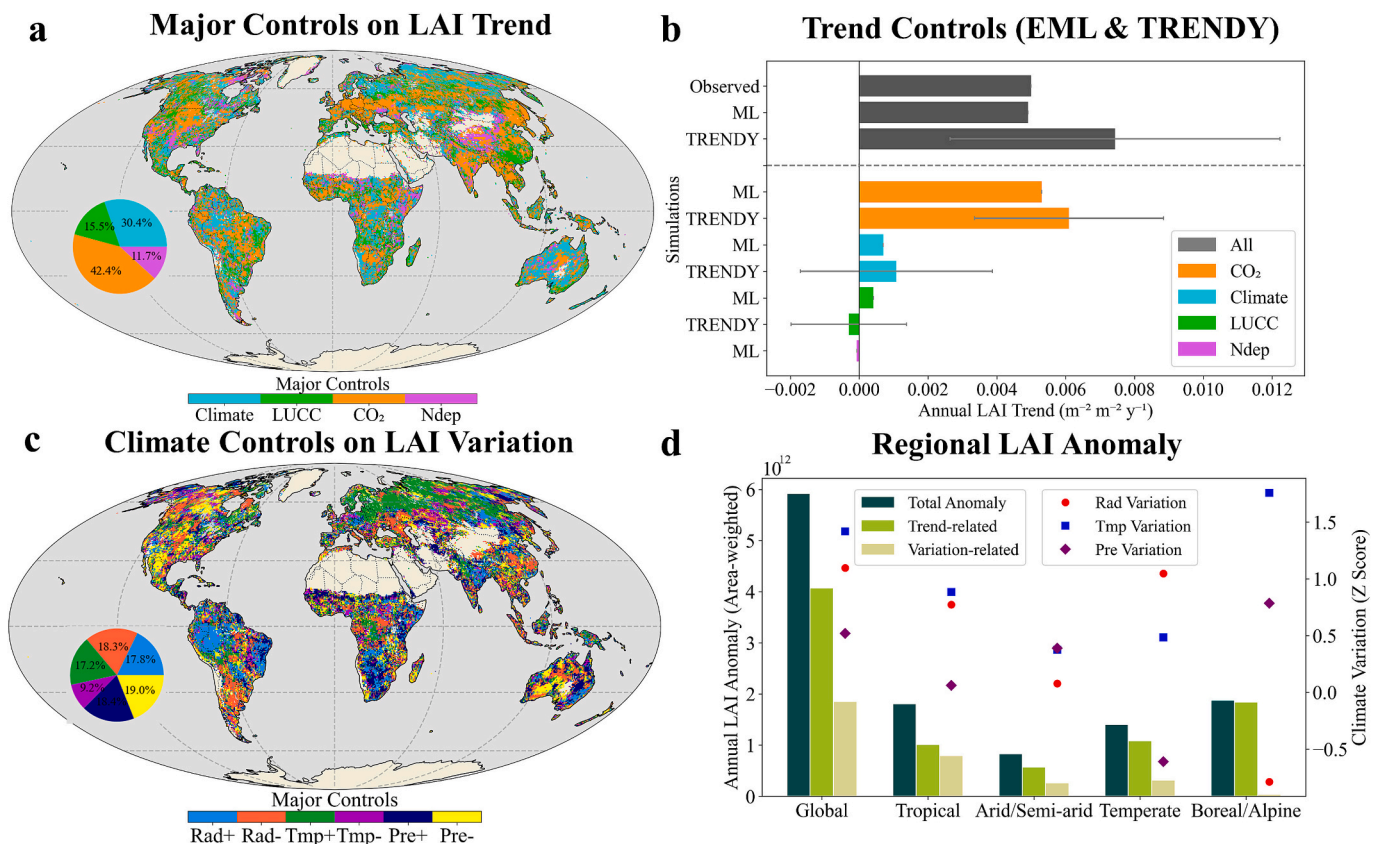

Fig. 4. Major controls on annual trend-related and variation-related anomalies of greenness in 2020 derived from the ensemble machine-learning (EML). **(a)** Major controls on annual LAI trend related to climate, land use/cover change (LUCC), CO_2 fertilization and nitrogen deposition (Ndep). **(b)** Comparison of annual LAI trend controls from EML and TRENDY. **(c)** EML-based climate controls on annual LAI variation in 2020. Three climatic factors are included: radiation (Rad), air temperature (Tmp) and precipitation (Pre). The symbols "+" and "-" represent positive and negative controls, respectively. The insect pie shows the relative area of each control to the global total vegetated area. **(d)** Comparison of annual LAI anomalies in 2020 (total anomaly and its two trend-related and variation-related componets) among different climate zones. Annual variations in three key climatic factors are shown by different symbols and quantified by the secondary axis.
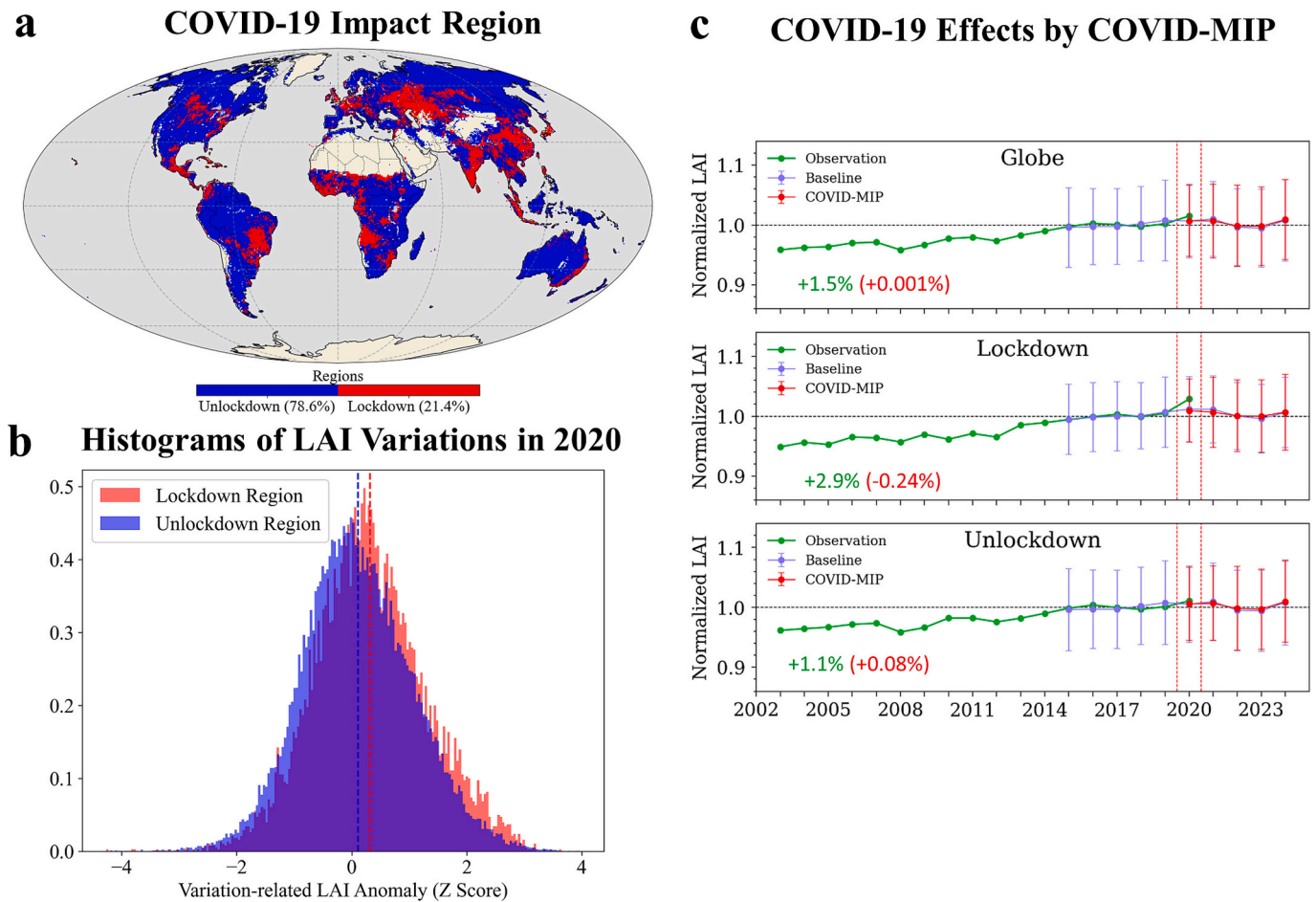
Fig. 5. Potential impact of COVID-19 lockdown on global vegetation greenness anomaly in 2020. (a) Identification of potential impact areas due to COVID-19 lockdown and travel restrictions. Their relative areas are shown by the percentage values in the legend. **(b)** Histograms of annual LAI variations in 2020 for lockdown and unlockdown regions. **(c)** COVID-19 effects on annual greenness anomalies simulated by COVID-MIP. The observation is from MODIS LAI. The baseline simulation is from CMIP6 under the SSP2–4.5 scenario. The difference between COVID-MIP and the baseline simulation represents the net effect of COVID-19. All LAIs are normalized by their multiple year average from 2015 and 2019. The observed LAI anomaly in 2020 relative to the multi-year mean is shown in green, with the COVID-19 effect marked in red in the parentheses. (For interpretation of the references to colour in this figure legend, the reader is referred to the web version of this article.)

respectively. Regarding the global trend-related anomaly, the boreal/alpine zone was most influential, contributing 40.8 %, while the arid/semi-arid zone was least at 12.7 %. For the variation-related anomaly, the tropical zone was predominant, contributing 56.4 %, with the boreal/alpine zone contributing the least at 2.7 %.

3.4. Limited effect of COVID-19 on global greening

The global lockdown status triggered by the COVID-19 pandemic in 2020 led to notable temporary reductions in air pollution and greenhouse gas emissions as well as human disturbances, which could in turn influence climate variability and vegetation anomaly. Utilizing satellite-based observations of ground-level NO_2, a sensitive indicator of air pollution, from TROPOMI, we identified approximately 21.4 % of global vegetated area as the direct impacted region by COVID-19 (Fig. 5a). This defined lockdown region generally aligns with the patterns of observed global air pollution reduction documented in earlier studies (Shrestha et al., 2020; Venter et al., 2020) and partially overlap with the most densely population area such as in China and Inida. However, both lockdown and unlock down regions showed heterogeneous patterns in annual greenness anomalies in 2020 (Fig. S13a & b). On a broad scale,

lockdown regions (+ 0.32 σ for annual LAI variation) exhibited a slightly greener than the unlock down region (+ 0.11 σ) (Fig. 5b), although their difference diminished as the time progressed, particularly in the second half of the year (Fig. S13).

We further examined land cover change in 2020 relative to 2019 and its effect on annual LAI anomaly in 2020 (Fig. S14). In the lockdown region, there was a net increase of 0.21 % for the averaged forest fraction and a net decrease of 0.1 % for averaged crop fraction. In contrast, the unlock region experienced a slightly decrease in forest fraction by 0.02 % and a smaller decrease in crop fraction by 0.07 %. As a result, the land cover changes had a positive effect on LAI (+ 0.02 σ) in the lockdown region, compared to a negative effect of −0.05 σ in the unlock region. However, these effects are much smaller than climate impacts on LAI, which were + 0.23 σ in the lockdown region and + 0.11 σ in the unlock region, largely due to wetting and warmer anomalies (Fig. S12).

Based on the model intercomparison project tailored to assess COVID-19 impacts (COVID-MIP), we found that the net effect of climate forcing from COVID-19 on global vegetation was notably limited, registering a mere +0.001 % change in LAI (Fig. 5c). When focusing on the lockdown region, the impact of COVID-19 was slightly more negative, showing a − 0.24 % change in LAI relative to the five-year mean.
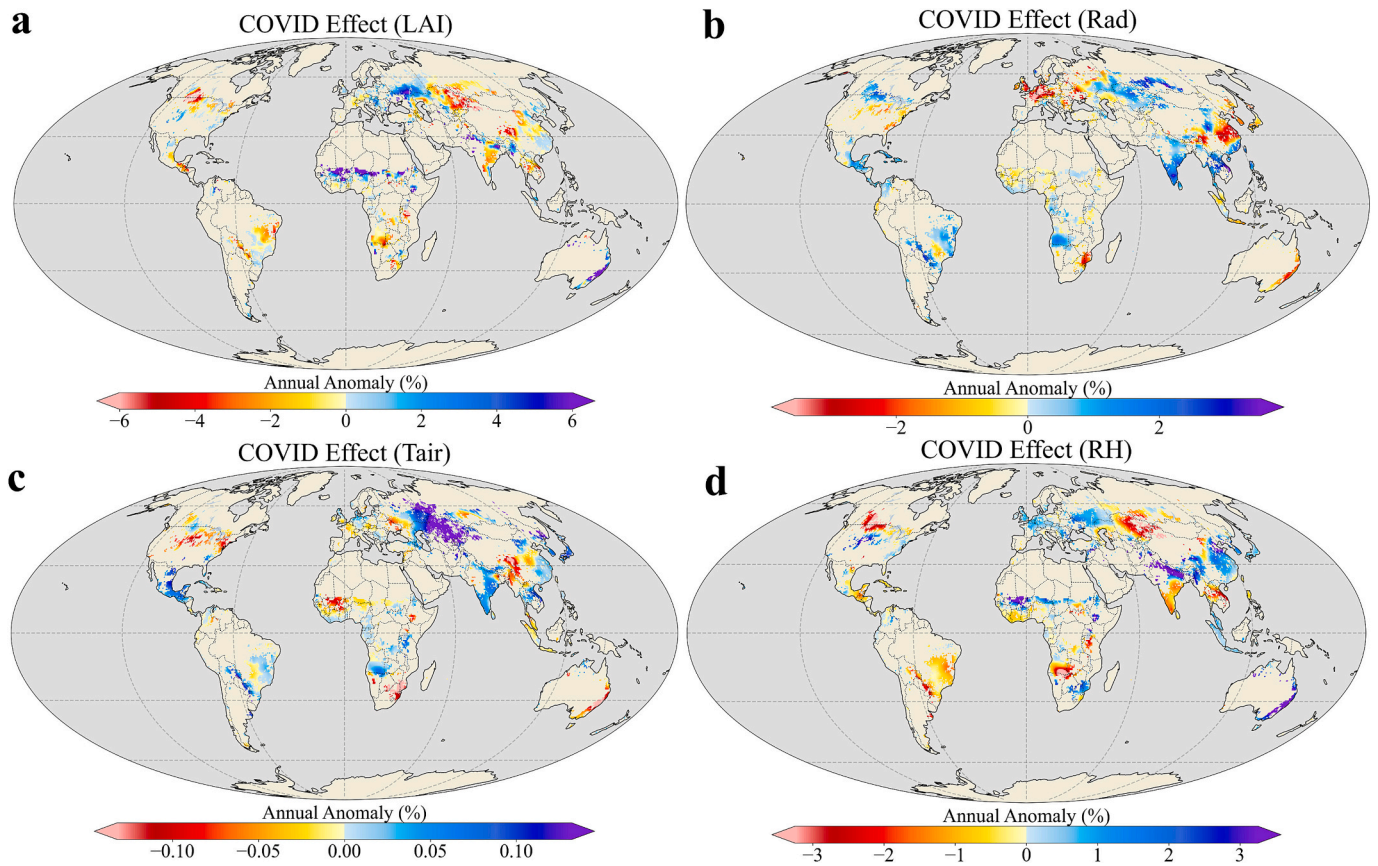
Fig. 6. Spatial patterns of net effects of COVID-19 on annual mean LAI (a), solar radiation (b), air temperature (Tair) (c) and relative humidity (RH) (d) over the lockdown region. The net effect is quantified by the difference between COVID-MIP and the baseline SSP2–4.5 scenario in 2020. To be consistent with Fig. 5c, the difference or annual anomaly is normalized by the mean of the baseline simulation from 2015 to 2019.

This contrasts with a smaller positive impact of +0.08 % in the unlock down regions. The simulated negative LAI by COVID-MIP (Fig. 6a) was related to a drying anomaly (Fig. 6d), which resulted from enhanced solar radiation (Fig. 6b) and climate warming (Fig. 6c) in response to the reduced anthropogenic greenhouse gas and pollution emissions due to the widespread lockdown (Lamboll et al., 2021). Interestingly, the COVID-19 induced climate forcing was generally opposite to the natural climate variability in 2020 (Fig. S12). However, the direct climate impacts from COVID-19 were much smaller when compared to the observed LAI anomalies (+2.9 % in lockdown regions and + 1.1 % in unlock down regions), indicating that the overall influence of COVID-19 on vegetation variations in 2020 was minor.

3.5. Global vegetation variability over the past two decades

To better understand the distinct nature of the 2020 greening anomaly, we contextualized it against the backdrop of vegetation variability observed over the past two decades (Fig. 7). Amidst an overarching trend of greening, we found that global vegetation in terms of MOD-LAI has exhibited significant variability during this period, underpinned by distinct contributions from various climate zones. The year 2020 showed the most pronounced positive variability (+1.45 σ), largely driven by the tropical zone, contrasting sharply with 2016 (+1.43 σ), when the temperate and boreal/alpine zones were more influential. Earlier, 2006 (+1.07 σ) and 2015 (+1.05 σ) witnessed
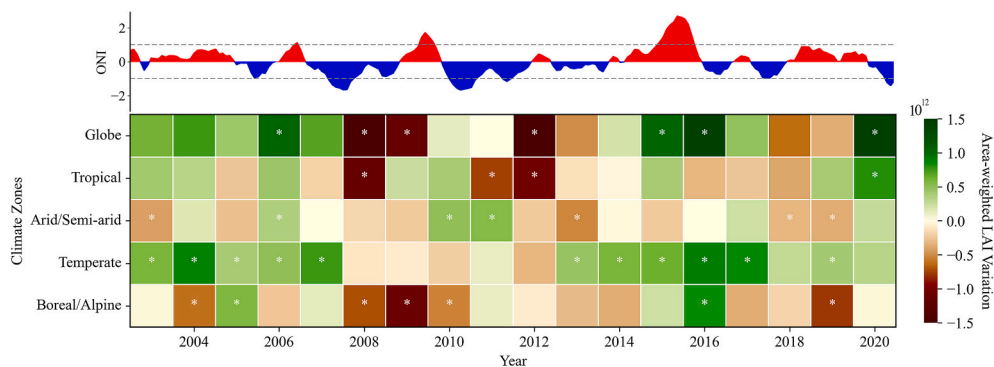

Fig. 7. Global vegetation variability contributed by different climate zones from 2003 to 2020. Annual area-weighted LAIs was detrended and detracted from their multi-year averages. Anomalies exceeding one standard deviation from the mean are marked by white asterisks. The upper figure shows the monthly Oceanic Niño Index (ONI), with positive values indicating a tendency towards El Niño, and negative values towards La Niña. The dashed lines indicate an ONI threshold of 1.0, above or below which represents moderate or strong El Niño or La Niña events.

significant contributions from the temperate zones. In contrast, years like 2008 (−2.17 σ), 2012 (−1.7 σ), and 2009 (−1.16 σ) experienced major negative variability, predominantly influenced by either tropical or boreal/alpine zones. Notably, extreme ENSO events exhibited connections with vegetation variability in specific climate zones, such as the tropical zone in 2020, the temperate zone during 2015–2016, and the arid/semi-arid zone in 2010–2011 (Fig. 7). However, these influences varied considerably, lacking uniformity and consistency both within and across zones. Overall, global vegetation displayed a recurring cycle, with peak greening occurring every 3–4 years, interspersed with browning events spanning 1–2 years, a rhythm found to be even more frequent in certain climate zones (Fig. S15). These marked variability in terrestrial vegetation ecosystems are anticipated to induce pronounced fluctuations in global carbon and water cycles.

4. Discussion

We observed a notable peak in global vegetation greening in 2020 by diverse remote sensing data (Fig. 2). This peak continues a sequence of similar phenomena previously recorded in 2007 (Zhang et al., 2017a, 2017b), 2011 (Poulter et al., 2014), and 2016 (Cao et al., 2023), fitting into a long-term greening trend since the early 2000s (Piao et al., 2020). This consistent pattern suggests a robust resilience and adaptability of global vegetation in the face of changing environmental conditions (Piao et al., 2020). However, the observed peak greening exhibited considerable spatial heterogeneity (Fig. 3), which is governed by a multifaceted mechanism (Fig. 4). Understanding these patterns and the mechanisms behind them is essential for projecting sustainability and evaluating potential risks linked to this encouraging greening trend (Piao et al., 2020).

Our study implemented a straightforward yet effective signal decomposition approach to unravel the interaction between potential long-term trends and short-term variability influencing the record greening in 2020. We found that the 2020 global greening anomaly was primarily attributed to the trend-related component (79 %; Fig. 1), which positively affected over 76 % of total vegetated area (Fig. 3). Our EML-based attribution confirmed the rising CO_2 as the major influencing factor for such trend-related anomaly, followed by climate change, LUCC and nitrogen deposition (Fig. 4b). Such a control order is generally consistent with land surface models from TRENDY (Sitch et al., 2015; Zhu et al., 2016). However, our EML-based approach showed a more extensive CO_2 control at the spatial scale, especially in temperate and arid/semi-arid zones (Fig. S10), diverging from the tropical-centric emphasis highlighted by TRENDY (Zhu et al., 2016; Piao et al., 2020). The rising CO_2 can directly enhance canopy photosynthesis through accelerated carboxylation, known as the 'CO_2 fertilization effect' or 'physiological effect' (Farquhar and Sharkey, 1982). This effect can further enhance vegetation greenness by causing partial closure of leaf stomata, thereby improving water-use efficiency (Keenan et al., 2013), a phenomenon particularly relevant in water-limited areas like semi-arid regions (Ukkola et al., 2016; Gentine et al., 2019). These complex, nonlinear processes may not be fully captured by the TRENDY models (Liu et al., 2019; Chen et al., 2022a, 2022b). Our findings, indicating a more extensive influence of CO_2, aligned with recent advancements in statistical modeling studies that similarly highlight this broader impact (Donohue et al., 2013; Huang et al., 2018). However, it should be noted that the rising CO_2 affects vegetation not only through 'physiological effect' but also 'radiative forcing effect'. The latter refers to the climate phenomenon that CO_2 concentrations tend to increase downward longwave radiation, leading to alterations in temperature and precipitation, and subsequently affecting plant growth (Winkler et al., 2021). The EML may not effectively separate these two effects, which could partially explain that TRRENDY tended to have a larger climate effect than EML (Fig. S10).

While occurring locally, LUCC exerted a significant control on the trend-related anomaly, impacting approximately16% of the total vegetated area, an extent about half of that affected by climate change (Fig. 4a). This is generally consistent with recent studies highlighting the pivotal roles of land use/cover change both at global (Arneth et al., 2017; Marques et al., 2019) and regional scales (Yu et al., 2019a, 2019b; Zhang et al., 2021). However, our EML-based attribution revealed a more extensive positive effect of LUCC in temperate regions, a conclusion that contrasts with simulations by TRENDY (Fig. S11). This greening in temperate zones is primarily attributed to widespread reforestation efforts in China (Yu et al., 2022) and/or the intensification of cropland (Chen et al., 2019), which appears to be underrepresented by the current TRENDY models (Piao et al., 2020; Park et al., 2023). It is worth noting that extensive cropland management practices such as irrigation, fertilization, and crop genetic modifications was not directly reflected in LUCC derived from MODIS products. Consequently, the CO_2 control over temperate croplands identified by both EML and TRENDY (Fig. S10) may be overestimated due to the underestimation of these human-dominated practices (Chen et al., 2019; Park et al., 2023). Nitrogen deposition exhibited dominant influences in some remote regions with sparse vegetation (Fig. 4a), suggesting that air pollution or wildfire smokes might positively affect these nitrogen-limited natural areas (Stevens et al., 2004; Bobbink et al., 2010). However, the extent and amplitude of such effects need further investigation through field control experiments (Du et al., 2020).

Our study demonstrated that instantaneous variation-related anomalies could lead to more pronounced and sometimes negative changes in vegetation activity compared to the more gradual trend-related changes (Fig. 3). The instantaneous anomaly, in comparison to the accumulated one, displayed almost twice the extent of negative patterns (46.3 % versus 23.3 %) and highlighted markedly stronger amplitudes in both its positive and negative manifestations (Fig. 3). Owing to the counteracting effects of these patterns, the overall contribution of the variation-related anomaly to the global total anomaly was comparatively smaller (Fig. 1). However, it exerted more pronounced influences on regional greening anomalies (Fig. 3). China, despite being a major contributor to global greening (Chen et al., 2019), exhibited a lower greenness anomaly (+1.35 σ) compared to India (+2.66 σ) in 2020 (Fig. S8). This greenness difference is primarily attributed to a substantially larger positive variation in India caused by a wetting anomaly, contrasted with a widespread negative variation in China caused by reduced radiation and/or partial drying anomaly (Figs. 3 & S12). This finding highlights the importance of considering both short-term variability and long-term trends when studying and managing vegetation dynamics and ecosystem health, particularly at the regional scales (Jung et al., 2017).

Although 2020 was recorded as the one of the warmest years in history (NASA, 2024), our EML-based simulations revealed that precipitation emerged as the dominant factor controlling the annual LAI variation in this year, affecting 37.4 % of the total area (Fig. 4c). This impact was on par with that of radiation control, which impacted 36.1 % of the area, and was more substantial than the effect of temperature control at 26.4 %. In specific regions like eastern Brazil, eastern Africa, and most of India, a strong wetting anomaly, combined with radiation variation, was identified as the key driver of the observed positive greenness anomaly. This regional wetting anomaly is likely to be linked with the strong 2019–2020 Indian Ocean Dipole and the moderate La Nina event in late 2020 (Weir et al., 2021). In regions like central Austria and North America, a substantial drying anomaly led to a negative greenness anomaly (Qin et al., 2022), whereas in southern China, a dimming condition was linked with decreased greenness (Chen et al., 2021). Conversely, in northern Eurasia, a warming anomaly played a role in enhancing greenness (Park et al., 2020). These diverse controls identified in our study highlight the complexity of climatic influences on ecosystems across the globe (Piao et al., 2020; Tang et al., 2020). The existing TRENDY models are unable to isolate the impact of individual climate factors on vegetation due to their configuration (Sitch et al., 2015). Our EML-based study offers a valuable supplement to address this limitation. However, it should be noted that while EML performed well

in simulating annual LAI values during the study period (Fig. S3), its ability to capture anomalies—small deviations after removing the multi-year mean baseline—was relatively weak (Table R3). Future improvements through refining temporal and spatial resolutions (e.g., seasonal scale at Landsat/Sentinel resolutions), including additional environmental predictors (e.g., climate extremes, root zone water content, and land management), incorporating more vegetation traits representing acclimation, state dependency and lag effects, and leveraging more advanced deep learning model architectures (e.g., LSTM, Transformer and their hybrid models) may help address this issue.

Despite COVID-19 lockdowns reduced air pollution (Venter et al., 2020) and human disturbances (Onyeaka et al., 2021), our study indicated that their overall impact on global vegetation was limited (Fig. 5), countering expectations of a major positive environmental shift on ecosystems due to reduced human activities (Diffenbaugh et al., 2020). We observed that lockdown regions exhibited a slight increase in greenness ($+0.32\,\sigma$ in LAI variation) compared to non-lockdown regions ($+0.11\,\sigma$), yet this disparity diminished over time (Fig. S13). A regional study highlighted a rapid greening response in China's spring vegetation to COVID-19 restrictions (Su et al., 2021), but our study indicated that this short-term effect was not sustained and ultimately did not alter the overall annual browning anomaly (Fig. S13). Possible reasons for this outcome might be linked to heightened secondary pollutions (such as haze and ozone pollutions) during the COVID-19 lockdown in China (Huang et al., 2021), which could have weakened the positive vegetation effect of COVID-19 (Su et al., 2021; Liu et al., 2024b). Although the slightly positive LUCC effect in the lockdown region (Fig. S14) aligns with the expectation of reduced disturbance due to the COVID-19 lockdown, directly attributing these LUCC to the lockdown is challenging. Based on fully coupled general circulation models from COVID-MIP (Lamboll et al., 2021), we further confirmed that the net effect of COVID-19 related to climate forcing on global LAI in 2020, encompassing both lockdown and unlock down regions, is marginal when compared to the natural variability (Fig. 5). However, COVID-MIP suggested that the simulated negative LAI effect over the lockdown region was linked to a warming-induced drying anomaly, which generally opposed the natural climate variability in 2020. This conclusion may need further validation based on independent Earth system model simulations given the uncertainty in COVID-MIP (Jones et al., 2021).

We observed a recurring cycle of peak greening in global vegetation every 3–4 years over recent decades (Fig. S15), marked by considerable inter-annual variability (Fig. 7). The year 2020 stood out with the most pronounced positive variability in global vegetation greenness, primarily contributed by the tropical zone (Fig. 7). However, earlier peak greening or browning years exhibited a variety of contributions from different climate zones, suggesting diverse vegetation responses at the regional scale. Extreme ENSO events were linked with vegetation variability in specific zones (Zhang et al., 2019a; Dannenberg et al., 2021), yet these influences varied widely (Fig. 7). Previous studies highlighted the influence of precipitation-sensitive areas such as arid/semi-arid zones on global vegetation dynamics (Poulter et al., 2014; Ahlström et al., 2015). However, we did not observe such a distinct role (Fig. 7), possibly due to the counteraction effects between the northern and southern hemispheres (Zhang et al., 2017a, 2017b; Ukkola et al., 2021; Liu et al., 2024a, 2024b).

Although our study primarily concentrates on the MODIS era with consistent satellite records, our conclusion that 2020 was the greenest year is supported by the newly released long-term AVHRR NDVI (Li et al., 2023b) and LAI (Cao et al., 2023) data, and the recent update of MODIS NDVI (Li et al., 2024), extending the observation period from 1982 to 2023. The exceptional greening of the Earth in 2020 represents a significant milestone in global vegetation's response to environmental changes. However, predicting the duration of this greening trend remains challenging, given the complex interplay of various drivers and the uncertainty of future climate scenarios (Zhao et al., 2020). Several factors, such as reduced carbon fertilization due to nitrogen limitation

(Wang et al., 2020), saturated water use efficiency due to increased vapor pressure deficit (Li et al., 2023a), intensified physiological drought from soil and atmospheric water stress (Novick et al., 2016; Li et al., 2023c), and enhanced anthropogenic disturbances (Miles and Kapos, 2008; Jones et al., 2018), could potentially slow down or even reverse this greening trend (Winkler et al., 2021; Liu et al., 2023a, 2023b). Notably, current global VI products still have uncertainties and exhibit inconsistent global vegetation signals, particularly at the inter-annual scale (Fig. S1). These discrepancies can arise from various factors, such as differences in VI features, sensor stability and calibration, algorithmic processing, and the methods used for gap-filling and cloud contamination correction (Jiang et al., 2017; Zhang et al., 2017a, 2017b). Continuously monitoring terrestrial vegetation dynamics at finer spatial and temporal scales (Xiao et al., 2021), while minimizing observation uncertainties (Zhang et al., 2017a, 2017b; Zeng et al., 2023), is essential for us to gain a comprehensive understanding of the health and sustainability of global vegetation.

Human-induced greenhouse gas emissions since the Industrial Revolution are widely recognized as the primary cause of the global climate crisis (Masson-Delmotte et al., 2021). The COVID-19 pandemic, as an indirect effect, led to an unprecedented reduction in these emissions due to global shutdowns and travel restrictions (Onyeaka et al., 2021). A key implication of our study is that the remarkable greening observed in 2020 could serve as an emerging constraint on the increase in global total carbon uptake by terrestrial vegetation through photosynthesis (Zhang et al., 2019b), offering insights into the stability and possible shift of the land carbon sink in one of the warmest recorded years (Duffy et al., 2021; García-Palacios et al., 2021). It will, in turn, enhance our understanding of the Earth's response to short-term greenhouse gas reductions during the pandemic (Lamboll et al., 2021) and aid in evaluating the accuracy of current models and observations in closing the Global Carbon Budget (Friedlingstein et al., 2022). Moreover, the substantial greening Earth in 2020 may be linked with the pulse of global water cycle by enhancing water consumption through transpiration (Yang et al., 2023) and further affecting reginal energy balances (Chen et al., 2020). The potential impacts and broader implications of these processes warrant further investigation. Finally, our multi-source remote sensing- and EML-based modeling and control attribution framework, along with the feasible anomaly decomposition methodology, can be readily used and serve as supplementary approaches for analyzing other climate essential variables[2].

5. Conclusions

Our study identified a notable peak in global vegetation greening in 2020 since the early 2000s using multi-source remote sensing indicators (EVI, SIF and LAI). Based on the anomaly signal decomposition, ensemble machine learning and process models from TRENDY, we found that the observed greening in 2020 was predominantly driven by increased tropical vegetation growth from enhanced rainfall, and further by a broader, long-term greening in boreal and temperate regions, linked with CO_2 fertilization, climate warming and reforestation. Despite the pandemic of COVID-19 lockdowns reducing air pollution and human disturbances, our study based on EML and COVID-MIP indicated that their overall impact on global vegetation anomaly in 2020 was limited. The exceptional greening observed in 2020 highlights the remarkable resilience and adaptability of global vegetation to environmental changes. However, forecasting the trajectory of this greening trend remains challenging due to the complex interactions among climate, vegetation and human activities. Continuous monitoring and advanced data-model fusions are essential to understand global vegetation dynamics and ecosystem health, thus informing effective climate mitigation strategies through optimized ecosystem

---

[2] https://gcos.wmo.int/en/essential-climate-variables/.

management.

CRediT authorship contribution statement

Yulong Zhang: Writing – review & editing, Writing – original draft, Visualization, Validation, Software, Resources, Methodology, Investigation, Formal analysis, Data curation, Conceptualization. **Jiafu Mao:** Writing – review & editing, Methodology, Funding acquisition, Formal analysis, Conceptualization. **Ge Sun:** Writing – review & editing, Resources, Project administration, Methodology. **Qinfeng Guo:** Writing – review & editing, Resources, Formal analysis. **Jeffrey Atkins:** Writing – review & editing, Resources. **Wenhong Li:** Writing – review & editing, Resources, Methodology. **Mingzhou Jin:** Writing – review & editing, Methodology. **Conghe Song:** Writing – review & editing, Resources, Methodology. **Jingfeng Xiao:** Resources, Methodology. **Taehee Hwang:** Writing – review & editing, Methodology. **Tong Qiu:** Writing – review & editing. **Lin Meng:** Writing – review & editing. **Daniel M. Ricciuto:** Writing – review & editing. **Xiaoying Shi:** Writing – review & editing. **Xing Li:** Writing – review & editing, Resources. **Peter Thornton:** Writing – review & editing. **Forrest Hoffman:** Writing – review & editing.

Declaration of competing interest

The authors declare that they have no known competing financial interests or personal relationships that could have appeared to influence the work reported in this paper.

Appendix A. Supplementary data

Supplementary data to this article can be found online at https://doi.org/10.1016/j.rse.2024.114494.

Data availability

All data needed to evaluate the conclusions in the paper are publicly available, with their respective access links provided in Table S1.

References

Abatzoglou, J.T., Dobrowski, S.Z., Parks, S.A., Hegewisch, K.C., 2018. TerraClimate, a high-resolution global dataset of monthly climate and climatic water balance from 1958–2015. Sci. Data 5, 1–12.

Abiodun, O.I., Jantan, A., Omolara, A.E., Dada, K.V., Mohamed, N.A., Arshad, H., 2018. State-of-the-art in artificial neural network applications: a survey. Heliyon 4, e00938.

Ahlström, A., Raupach, M.R., Schurgers, G., Smith, B., Arneth, A., Jung, M., Reichstein, M., Canadell, J.G., Friedlingstein, P., Jain, A.K., Kato, E., Poulter, B., Sitch, S., Stocker, B.D., Viovy, N., Wang, Y.P., Wiltshire, A., Zaehle, S., Zeng, N., 2015. The dominant role of semi-arid ecosystems in the trend and variability of the land CO_2 sink. Science 348, 895–899. https://doi.org/10.1126/science.aaa1668.

Arneth, A., Sitch, S., Pongratz, J., Stocker, B.D., Ciais, P., Poulter, B., Bayer, A.D., Bondeau, A., Calle, L., Chini, L.P., 2017. Historical carbon dioxide emissions caused by land-use changes are possibly larger than assumed. Nat. Geosci. 10, 79–84.

Bastos, A., O'Sullivan, M., Ciais, P., Makowski, D., Sitch, S., Friedlingstein, P., Chevallier, F., Rödenbeck, C., Pongratz, J., Luijkx, I.T., Patra, P.K., Peylin, P., Canadell, J.G., Lauerwald, R., Li, W., Smith, N.E., Peters, W., Goll, D.S., Jain, A.K., Kato, E., Lienert, S., Lombardozzi, D.L., Haverd, V., Nabel, J.E.M.S., Poulter, B., Tian, H., Walker, A.P., Zaehle, S., 2020. Sources of uncertainty in regional and global terrestrial CO_2 exchange estimates. Glob. Biogeochem. Cycles 34. https://doi.org/10.1029/2019GB006393.

Beck, H.E., Zimmermann, N.E., McVicar, T.R., Vergopolan, N., Berg, A., Wood, E.F., 2018. Present and future Köppen-Geiger climate classification maps at 1-km resolution. Sci. Data 5, 1–12.

Beer, C., Reichstein, M., Tomelleri, E., Ciais, P., Jung, M., Carvalhais, N., Rödenbeck, C., Arain, M.A., Baldocchi, D., Bonan, G.B., 2010. Terrestrial gross carbon dioxide uptake: global distribution and covariation with climate. Science 329, 834–838.

Bobbink, R., Hicks, K., Galloway, J., Spranger, T., Alkemade, R., Ashmore, M., Bustamante, M., Cinderby, S., Davidson, E., Dentener, F., 2010. Global assessment of nitrogen deposition effects on terrestrial plant diversity: a synthesis. Ecol. Appl. 20, 30–59.

Breiman, L., 2001. Random forests. Mach. Learn. 45, 5–32.

Canadell, J.G., Raupach, M.R., 2008. Managing forests for climate change mitigation. science 320, 1456–1457.

Cao, S., Li, M., Zhu, Z., Wang, Z., Zha, J., Zhao, W., Duanmu, Z., Chen, J., Zheng, Y., Chen, Y., 2023. Spatiotemporally consistent global dataset of the GIMMS leaf area index (GIMMS LAI4g) from 1982 to 2020. Earth Syst. Sci. Data 15, 4877–4899.

Caruana, R., Niculescu-Mizil, A., Crew, G., Ksikes, A., 2004. Ensemble selection from libraries of models. In: Twenty-First International Conference on Machine Learning - ICML '04. Presented at the Twenty-First International Conference. ACM Press, Banff, Alberta, Canada, p. 18. https://doi.org/10.1145/1015330.1015432.

Chen, T., Guestrin, C., 2016. Xgboost: a scalable tree boosting system. In: Presented at the Proceedings of the 22nd acm Sigkdd International Conference on Knowledge Discovery and Data Mining, pp. 785–794.

Chen, C., Park, T., Wang, X., Piao, S., Xu, B., Chaturvedi, R.K., Fuchs, R., Brovkin, V., Ciais, P., Fensholt, R., Tømmervik, H., Bala, G., Zhu, Z., Nemani, R.R., Myneni, R.B., 2019. China and India lead in greening of the world through land-use management. Nat. Sustain. 2, 122–129. https://doi.org/10.1038/s41893-019-0220-7.

Chen, C., Li, D., Li, Y., Piao, S., Wang, X., Huang, M., Gentine, P., Nemani, R.R., Myneni, R.B., 2020. Biophysical impacts of earth greening largely controlled by aerodynamic resistance. Sci. Adv. 6, eabb1981.

Chen, S., Zhang, Y., Wu, Q., Liu, S., Song, C., Xiao, J., Band, L.E., Vose, J.M., 2021. Vegetation structural change and CO2 fertilization more than offset gross primary production decline caused by reduced solar radiation in China. Agric. For. Meteorol. 296, 108207.

Chen, X., Huang, Y., Nie, C., Zhang, S., Wang, G., Chen, S., Chen, Z., 2022a. A long-term reconstructed TROPOMI solar-induced fluorescence dataset using machine learning algorithms. Sci. Data 9, 427. https://doi.org/10.1038/s41597-022-01520-1.

Chen, C., Riley, W.J., Prentice, I.C., Keenan, T.F., 2022b. CO2 fertilization of terrestrial photosynthesis inferred from site to global scales. Proc. Natl. Acad. Sci. 119, e2115627119.

Ciotti, M., Ciccozzi, M., Terrinoni, A., Jiang, W.-C., Wang, C.-B., Bernardini, S., 2020. The COVID-19 pandemic. Crit. Rev. Clin. Lab. Sci. 57, 365–388.

Dannenberg, M.P., Smith, W.K., Zhang, Y., Song, C., Huntzinger, D.N., Moore, D.J., 2021. Large-scale reductions in terrestrial carbon uptake following Central Pacific El Niño. Geophys. Res. Lett. 48, e2020GL092367.

Diffenbaugh, N.S., Field, C.B., Appel, E.A., Azevedo, I.L., Baldocchi, D.D., Burke, M., Burney, J.A., Ciais, P., Davis, S.J., Fiore, A.M., Fletcher, S.M., Hertel, T.W., Horton, D.E., Hsiang, S.M., Jackson, R.B., Jin, X., Levi, M., Lobell, D.B., McKinley, G.A., Moore, F.C., Montgomery, A., Nadeau, K.C., Pataki, D.E., Randerson, J.T., Reichstein, M., Schnell, J.L., Seneviratne, S.I., Singh, D., Steiner, A.L., Wong-Parodi, G., 2020. The COVID-19 lockdowns: a window into the earth system. Nat. Rev. Earth Environ. 1, 470–481. https://doi.org/10.1038/s43017-020-0079-1.

Donohue, R.J., Roderick, M.L., McVicar, T.R., Farquhar, G.D., 2013. Impact of CO2 fertilization on maximum foliage cover across the globe's warm, arid environments. Geophys. Res. Lett. 40, 3031–3035.

Du, E., Terrer, C., Pellegrini, A.F., Ahlström, A., van Lissa, C.J., Zhao, X., Xia, N., Wu, X., Jackson, R.B., 2020. Global patterns of terrestrial nitrogen and phosphorus limitation. Nat. Geosci. 13, 221–226.

Duffy, K.A., Schwalm, C.R., Arcus, V.L., Koch, G.W., Liang, L.L., Schipper, L.A., 2021. How close are we to the temperature tipping point of the terrestrial biosphere? Sci. Adv. 7, eaay1052.

Falkowski, P., Scholes, R.J., Boyle, E.E.A., Canadell, J., Canfield, D., Elser, J., Gruber, N., Hibbard, K., Högberg, P., Linder, S., 2000. The global carbon cycle: a test of our knowledge of earth as a system. Science 290, 291–296.

Fang, H., Baret, F., Plummer, S., Schaepman-Strub, G., 2019. An overview of global leaf area index (LAI): methods, products, validation, and applications. Rev. Geophys. 57, 739–799.

Farquhar, G.D., Sharkey, T.D., 1982. Stomatal conductance and photosynthesis. Annu. Rev. Plant Physiol. 33, 317–345.

Fernandes, R., Leblanc, S.G., 2005. Parametric (modified least squares) and non-parametric (Theil–Sen) linear regressions for predicting biophysical parameters in the presence of measurement errors. Remote Sens. Environ. 95, 303–316.

Forzieri, G., Miralles, D.G., Ciais, P., Alkama, R., Ryu, Y., Duveiller, G., Zhang, K., Robertson, E., Kautz, M., Martens, B., 2020. Increased control of vegetation on global terrestrial energy fluxes. Nat. Clim. Chang. 10, 356–362.

Friedlingstein, P., O`Sullivan, M., Jones, M.W., Andrew, R.M., Gregor, L., Hauck, J., 2022. Global carbon budget 2022. Earth Syst. Sci. Data 14, 4811–4900.

García-Palacios, P., Crowther, T.W., Dacal, M., Hartley, I.P., Reinsch, S., Rinnan, R., Rousk, J., van den Hoogen, J., Ye, J.-S., Bradford, M.A., 2021. Evidence for large microbial-mediated losses of soil carbon under anthropogenic warming. Nat. Rev. Earth & Environ. 2, 507–517.

Gentine, P., Green, J.K., Guérin, M., Humphrey, V., Seneviratne, S.I., Zhang, Y., Zhou, S., 2019. Coupling between the terrestrial carbon and water cycles—a review. Environ. Res. Lett. 14, 083003.

Green, J.K., Konings, A.G., Alemohammad, S.H., Berry, J., Entekhabi, D., Kolassa, J., Lee, J.-E., Gentine, P., 2017. Regionally strong feedbacks between the atmosphere and terrestrial biosphere. Nat. Geosci. 10, 410–414.

Griscom, B.W., Adams, J., Ellis, P.W., Houghton, R.A., Lomax, G., Miteva, D.A., Schlesinger, W.H., Shoch, D., Siikamäki, J.V., Smith, P., 2017. Natural climate solutions. Proc. Natl. Acad. Sci. 114, 11645–11650.

Huang, K., Xia, J., Wang, Y., Ahlström, A., Chen, J., Cook, R.B., Cui, E., Fang, Y., Fisher, J.B., Huntzinger, D.N., Li, Z., Michalak, A.M., Qiao, Y., Schaefer, K., Schwalm, C., Wang, J., Wei, Y., Xu, X., Yan, L., Bian, C., Luo, Y., 2018. Enhanced peak growth of global vegetation and its key mechanisms. Nat. Ecol. Evol. 2, 1897–1905. https://doi.org/10.1038/s41559-018-0714-0.

Huang, X., Ding, A., Gao, J., Zheng, B., Zhou, D., Qi, X., Tang, R., Wang, J., Ren, C., Nie, W., 2021. Enhanced secondary pollution offset reduction of primary emissions during COVID-19 lockdown in China. Natl. Sci. Rev. 8, nwaa137.

Huete, A., Didan, K., Miura, T., Rodriguez, E.P., Gao, X., Ferreira, L.G., 2002. Overview of the radiometric and biophysical performance of the MODIS vegetation indices. Remote Sens. Environ. 83, 195–213.

Imhoff, M.L., Bounoua, L., Ricketts, T., Loucks, C., Harriss, R., Lawrence, W.T., 2004. Global patterns in human consumption of net primary production. Nature 429, 870–873.

Jiang, C., Ryu, Y., Fang, H., Myneni, R., Claverie, M., Zhu, Z., 2017. Inconsistencies of interannual variability and trends in long-term satellite leaf area index products. Glob. Chang. Biol. 23 (10), 4133–4146.

Jones, K.R., Venter, O., Fuller, R.A., Allan, J.R., Maxwell, S.L., Negret, P.J., Watson, J.E., 2018. One-third of global protected land is under intense human pressure. Science 360, 788–791.

Jones, Chris D., Hickman, Jonathan E., Rumbold, Steven T., Walton, Jeremy, Lamboll, Robin D., Skeie, Ragnhild B., Fiedler, Stephanie, et al., 2021. The climate response to emissions reductions due to COVID-19: initial results from CovidMIP. Geophys. Res. Lett. 48, no. 8, e2020GL091883.

Jung, M., Reichstein, M., Schwalm, C.R., Huntingford, C., Sitch, S., Ahlström, A., Arneth, A., Camps-Valls, G., Ciais, P., Friedlingstein, P., Gans, F., Ichii, K., Jain, A.K., Kato, E., Papale, D., Poulter, B., Raduly, B., Rödenbeck, C., Tramontana, G., Viovy, N., Wang, Y.-P., Weber, U., Zaehle, S., Zeng, N., 2017. Compensatory water effects link yearly global land CO2 sink changes to temperature. Nature 541, 516–520. https://doi.org/10.1038/nature20780.

Ke, G., Meng, Q., Finley, T., Wang, T., Chen, W., Ma, W., Ye, Q., Liu, T.-Y., 2017. Lightgbm: a highly efficient gradient boosting decision tree. Adv. Neural Inf. Proces. Syst. 30.

Keenan, T.F., Riley, W.J., 2018. Greening of the land surface in the world's cold regions consistent with recent warming. Nat. Clim. Chang. 8, 825–828.

Keenan, T.F., Hollinger, D.Y., Bohrer, G., Dragoni, D., Munger, J.W., Schmid, H.P., Richardson, A.D., 2013. Increase in forest water-use efficiency as atmospheric carbon dioxide concentrations rise. Nature 499, 324–327.

Krause, A.G., Weis, E., 1991. Chlorophyll fluorescence and photosynthesis: the basics. Annu. Rev. Plant Biol. 42, 313–349.

Lamboll, R.D., Jones, C.D., Skeie, R.B., Fiedler, S., Samset, B.H., Gillett, N.P., Rogelj, J., Forster, P.M., 2021. Modifying emissions scenario projections to account for the effects of COVID-19: protocol for CovidMIP. Geosci. Model Dev. 14, 3683–3695.

Li, X., Xiao, J., 2019. A global, 0.05-degree product of solar-induced chlorophyll fluorescence derived from OCO-2, MODIS, and reanalysis data. Remote Sens. 11, 517.

Li, F., Xiao, J., Chen, J., Ballantyne, A., Jin, K., Li, B., Abraha, M., John, R., 2023a. Global water use efficiency saturation due to increased vapor pressure deficit. Science 381, 672–677.

Li, M., Cao, S., Zhu, Z., Wang, Z., Myneni, R.B., Piao, S., 2023b. Spatiotemporally consistent global dataset of the GIMMS normalized difference vegetation index (PKU GIMMS NDVI) from 1982 to 2022. Earth Syst. Sci. Data 15, 4181–4203.

Li, W., Pacheco-Labrador, J., Migliavacca, M., Miralles, D., Hoek van Dijke, A., Reichstein, M., Forkel, M., Zhang, W., Frankenberg, C., Panwar, A., 2023c. Widespread and complex drought effects on vegetation physiology inferred from space. Nat. Commun. 14, 4640.

Li, X., Wang, K., Huntingford, C., Zhu, Z., Peñuelas, J., Myneni, R.B., Piao, S., 2024. Vegetation greenness in 2023. Nat. Rev. Earth & Environ. 5 (4), 241–243.

Liang, X., Liu, Q., Wang, J., Chen, S., Gong, P., 2024. Global 500 m seamless dataset (2000–2022) of land surface reflectance generated from MODIS products. Earth Syst. Sci. Data 16, 177–200. https://doi.org/10.5194/essd-16-177-2024.

Liu, Y., Liu, R., Chen, J.M., 2012. Retrospective retrieval of long-term consistent global leaf area index (1981–2011) from combined AVHRR and MODIS data. Journal of geophysical research. Biogeosciences 117.

Liu, Y., Piao, S., Gasser, T., Ciais, P., Yang, H., Wang, H., Keenan, T.F., Huang, Mengtian, Wan, S., Song, J., Wang, K., Janssens, I.A., Peñuelas, J., Huntingford, C., Wang, X., Altaf Arain, M., Fang, Y., Fisher, J.B., Huang, Maoyi, Huntzinger, D.N., Ito, A., Jain, A.K., Mao, J., Michalak, A.M., Peng, C., Poulter, B., Schwalm, C., Shi, X., Tian, H., Wei, Y., Zeng, N., Zhu, Q., Wang, T., 2019. Field-experiment constraints on the enhancement of the terrestrial carbon sink by CO2 fertilization. Nat. Geosci. 12, 809–814. https://doi.org/10.1038/s41561-019-0436-1.

Liu, Z., Ciais, P., Deng, Z., Lei, R., Davis, S.J., Feng, S., Zheng, B., Cui, D., Dou, X., Zhu, B., 2020. Near-real-time monitoring of global CO2 emissions reveals the effects of the COVID-19 pandemic. Nat. Commun. 11, 5172.

Liu, Z., Deng, Z., Zhu, B., Ciais, P., Davis, S.J., Tan, J., Andrew, R.M., Boucher, O., Arous, S.B., Canadell, J.G., 2022. Global patterns of daily CO2 emissions reductions in the first year of COVID-19. Nat. Geosci. 15, 615–620.

Liu, Q., Peng, C., Schneider, R., Cyr, D., Liu, Z., Zhou, X., Du, M., Li, P., Jiang, Z., McDowell, N.G., 2023a. Vegetation browning: global drivers, impacts, and feedbacks. Trends Plant Sci. 28 (9), 1014–1032.

Liu, X., Sun, G., Fu, Z., Ciais, P., Feng, X., Li, J., Fu, B., 2023b. Compound droughts slow down the greening of the earth. Glob. Chang. Biol. 29, 3072–3084.

Liu, J., Baker, D., Basu, S., Bowman, K., Byrne, B., Chevallier, F., He, W., Jiang, F., Johnson, M.S., Kubar, T.L., Li, X., 2024a. The reduced net carbon uptake over northern hemisphere land causes the close-to-normal CO2 growth rate in 2021 La Niña. Sci. Adv. 10 (23), eadl2201.

Liu, X., Chu, B., Tang, R., Liu, Y., Qiu, B., Gao, M., Li, X., Xiao, J., Sun, H.Z., Huang, X., 2024b. Air quality improvements can strengthen China's food security. Nat. Food 1–13.

Mao, J., Ribes, A., Yan, B., Shi, X., Thornton, P.E., Séférian, R., Ciais, P., Myneni, R.B., Douville, H., Piao, S., 2016. Human-induced greening of the northern extratropical land surface. Nat. Clim. Chang. 6, 959–963.

Marques, A., Martins, I.S., Kastner, T., Plutzar, C., Theurl, M.C., Eisenmenger, N., Huijbregts, M.A., Wood, R., Stadler, K., Bruckner, M., 2019. Increasing impacts of land use on biodiversity and carbon sequestration driven by population and economic growth. Nat. Ecol. & Evolut. 3, 628–637.

Masson-Delmotte, V.P., Zhai, P., Pirani, S.L., Connors, C., Péan, S., Berger, N., Caud, Y., Chen, L., Goldfarb, M.I., Scheel Monteiro, P.M., 2021. Ipcc, 2021: summary for policymakers. In: Climate Change 2021: the Physical Science Basis. Contribution of Working Group i to the Sixth Assessment report of the Intergovernmental Panel on Climate Change.

Matricardi, E.A.T., Skole, D.L., Costa, O.B., Pedlowski, M.A., Samek, J.H., Miguel, E.P., 2020. Long-term forest degradation surpasses deforestation in the Brazilian Amazon. Science 369, 1378–1382.

Mauritsen, T., Bader, J., Becker, T., Behrens, J., Bittner, M., Brokopf, R., Brovkin, V., Claussen, M., Crueger, T., Esch, M., 2019. Developments in the MPI-M earth system model version 1.2 (MPI-ESM1. 2) and its response to increasing CO2. J. Adv. Model. Earth Syst. 11, 998–1038.

Miles, L., Kapos, V., 2008. Reducing greenhouse gas emissions from deforestation and forest degradation: global land-use implications. science 320, 1454–1455.

NASA, 2024. GISS Surface Temperature Analysis (v4).

Novick, K.A., Ficklin, D.L., Stoy, P.C., Williams, C.A., Bohrer, G., Oishi, A.C., Papuga, S. A., Blanken, P.D., Noormets, A., Sulman, B.N., 2016. The increasing importance of atmospheric demand for ecosystem water and carbon fluxes. Nat. Clim. Chang. 6, 1023–1027.

Onyeaka, H., Anumudu, C.K., Al-Sharify, Z.T., Egele-Godswill, E., Mbaegbu, P., 2021. COVID-19 pandemic: a review of the global lockdown and its far-reaching effects. Sci. Prog. 104, 00368504211019854.

Pan, N., Feng, X., Fu, B., Wang, S., Ji, F., Pan, S., 2018. Increasing global vegetation browning hidden in overall vegetation greening: insights from time-varying trends. Remote Sens. Environ. 214, 59–72.

Park, H., Jeong, S., Peñuelas, J., 2020. Accelerated rate of vegetation green-up related to warming at northern high latitudes. Glob. Chang. Biol. 26, 6190–6202.

Park, T., Gumma, M.K., Wang, W., Panjala, P., Dubey, S.K., Nemani, R.R., 2023. Greening of human-dominated ecosystems in India. Communicat. Earth & Environ. 4 (1), 419.

Piao, S., Wang, X., Park, T., Chen, C., Lian, X., He, Y., Bjerke, J.W., Chen, A., Ciais, P., Tømmervik, H., Nemani, R.R., Myneni, R.B., 2020. Characteristics, drivers and feedbacks of global greening. Nat. Rev. Earth Environ. 1, 14–27. https://doi.org/10.1038/s43017-019-0001-x.

Pimm, S.L., Lawton, J.H., Cohen, J.E., 1991. Food web patterns and their consequences. Nature 350, 669–674.

Poulter, B., Frank, D., Ciais, P., Myneni, R.B., Andela, N., Bi, J., Broquet, G., Canadell, J. G., Chevallier, F., Liu, Y.Y., Running, S.W., Sitch, S., van der Werf, G.R., 2014. Contribution of semi-arid ecosystems to interannual variability of the global carbon cycle. Nature 509, 600–603. https://doi.org/10.1038/nature13376.

Prokhorenkova, L., Gusev, G., Vorobev, A., Dorogush, A.V., Gulin, A., 2018. CatBoost: unbiased boosting with categorical features. Advances in neural information processing systems, 31.

Qin, Y., Xiao, X., Wigneron, J.-P., Ciais, P., Canadell, J.G., Brandt, M., Li, X., Fan, L., Wu, X., Tang, H., 2022. Large loss and rapid recovery of vegetation cover and

aboveground biomass over forest areas in Australia during 2019–2020. Remote Sens. Environ. 278, 113087.

Roscher, R., Bohn, B., Duarte, M.F., Garcke, J., 2020. Explainable machine learning for scientific insights and discoveries. Ieee Access 8, 42200–42216.

Running, S.W., 2012. A measurable planetary boundary for the biosphere. science 337, 1458–1459.

Sagi, O., Rokach, L., 2018. Ensemble learning: a survey. In: Wiley Interdisciplinary Reviews: Data Mining and Knowledge Discovery, 8, p. e1249.

Shrestha, A., Shrestha, U., Sharma, R., Bhattarai, S., Tran, H., Rupakheti, M., 2020. Lockdown caused by COVID-19 pandemic reduces air pollution in cities worldwide (preprint). Life Sci. https://doi.org/10.31223/OSF.IO/EDT4J.

Sitch, S., Friedlingstein, P., Gruber, N., Jones, S.D., Murray-Tortarolo, G., Ahlström, A., Doney, S.C., Graven, H., Heinze, C., Huntingford, C., 2015. Recent trends and drivers of regional sources and sinks of carbon dioxide. Biogeosciences 12, 653–679.

Stevens, C.J., Dise, N.B., Mountford, J.O., Gowing, D.J., 2004. Impact of nitrogen deposition on the species richness of grasslands. Science 303, 1876–1879.

Su, F., Fu, D., Yan, F., Xiao, H., Pan, T., Xiao, Y., Kang, L., Zhou, C., Meadows, M., Lyne, V., Wilson, J.P., Zhao, N., Yang, X., Liu, G., 2021. Rapid greening response of China's 2020 spring vegetation to COVID-19 restrictions: implications for climate change. Sci. Adv. 7, eabe8044. https://doi.org/10.1126/sciadv.abe8044.

Sulla-Menashe, D., Gray, J.M., Abercrombie, S.P., Friedl, M.A., 2019. Hierarchical mapping of annual global land cover 2001 to present: the MODIS collection 6 land cover product. Remote Sens. Environ. 222, 183–194.

Sun, Y., Gu, L., Wen, J., van Der Tol, C., Porcar-Castell, A., Joiner, J., Chang, C.Y., Magney, T., Wang, L., Hu, L., Rascher, U., 2023. From remotely sensed solar-induced chlorophyll fluorescence to ecosystem structure, function, and service: part I—harnessing theory. Glob. Chang. Biol. 29 (11), 2926–2952.

Tang, S., Wang, X., He, M., Huang, L., Zhang, Y., Yang, H., Piao, S., 2020. Global patterns and climate controls of terrestrial ecosystem light use efficiency. J. Geophys. Res. Biogeosci. 125. https://doi.org/10.1029/2020JG005908.

Tramontana, G., Jung, M., Schwalm, C.R., Ichii, K., Camps-Valls, G., Ráduly, B., Reichstein, M., Arain, M.A., Cescatti, A., Kiely, G., Merbold, L., Serrano-Ortiz, P., Sickert, S., Wolf, S., Papale, D., 2016. Predicting carbon dioxide and energy fluxes across global FLUXNET sites with regression algorithms. Biogeosciences 13, 4291–4313. https://doi.org/10.5194/bg-13-4291-2016.

Ukkola, A.M., Prentice, I.C., Keenan, T.F., Van Dijk, A.I., Viney, N.R., Myneni, R.B., Bi, J., 2016. Reduced streamflow in water-stressed climates consistent with CO2 effects on vegetation. Nat. Clim. Chang. 6, 75–78.

Ukkola, A.M., De Kauwe, M.G., Roderick, M.L., Burrell, A., Lehmann, P., Pitman, A.J., 2021. Annual precipitation explains variability in dryland vegetation greenness globally but not locally. Glob. Chang. Biol. 27, 4367–4380.

Venter, Z.S., Aunan, K., Chowdhury, S., Lelieveld, J., 2020. COVID-19 lockdowns cause global air pollution declines. Proc. Natl. Acad. Sci. 117, 18984–18990.

Vicente-Serrano, S.M., Gouveia, C., Camarero, J.J., Beguería, S., Trigo, R., López-Moreno, J.I., Azorín-Molina, C., Pasho, E., Lorenzo-Lacruz, J., Revuelto, J., 2013. Response of vegetation to drought time-scales across global land biomes. Proc. Natl. Acad. Sci. 110, 52–57.

Wang, S., Zhang, Y., Ju, W., Chen, J.M., Ciais, P., Cescatti, A., Sardans, J., Janssens, I.A., Wu, M., Berry, J.A., 2020. Recent global decline of CO2 fertilization effects on vegetation photosynthesis. Science 370, 1295–1300.

Weir, B., Crisp, D., O'Dell, C.W., Basu, S., Chatterjee, A., Kolassa, J., Oda, T., Pawson, S., Poulter, B., Zhang, Z., Ciais, P., Davis, S.J., Liu, Z., Ott, L.E., 2021. Regional impacts of COVID-19 on carbon dioxide detected worldwide from space. Sci. Adv. 7, eabf9415. https://doi.org/10.1126/sciadv.abf9415.

Winkler, A.J., Myneni, R.B., Hannart, A., Sitch, S., Haverd, V., Lombardozzi, D., Arora, V. K., Pongratz, J., Nabel, J.E.M.S., Goll, D.S., Kato, E., Tian, H., Arneth, A., Friedlingstein, P., Jain, A.K., Zaehle, S., Brovkin, V., 2021. Slowdown of the greening

trend in natural vegetation with further rise in atmospheric CO2. Biogeosciences 18, 4985–5010. https://doi.org/10.5194/bg-18-4985-2021.

Xiao, J., Fisher, J.B., Hashimoto, H., Ichii, K., Parazoo, N.C., 2021. Emerging satellite observations for diurnal cycling of ecosystem processes. Nature Plants 7, 877–887.

Yan, K., Park, T., Yan, G., Chen, C., Yang, B., Liu, Z., Nemani, R.R., Knyazikhin, Y., Myneni, R.B., 2016. Evaluation of MODIS LAI/FPAR product collection 6. Part 1: consistency and improvements. Remote Sens. 8 (5), 359.

Yang, Y., Roderick, M.L., Guo, H., Miralles, D.G., Zhang, L., Fatichi, S., Luo, X., Zhang, Y., McVicar, T.R., Tu, Z., 2023. Evapotranspiration on a greening earth. Nat. Rev. Earth & Environ. 4, 626–641.

Yu, Z., Lu, C., Tian, H., Canadell, J.G., 2019a. Largely underestimated carbon emission from land use and land cover change in the conterminous United States. Glob. Chang. Biol. 25, 3741–3752.

Yu, L., Wen, J., Chang, C., Frankenberg, C., Sun, Y., 2019b. High-resolution global contiguous SIF of OCO-2. Geophys. Res. Lett. 46, 1449–1458.

Yu, Z., Ciais, P., Piao, S., Houghton, R.A., Lu, C., Tian, H., Agathokleous, E., Kattel, G.R., Sitch, S., Goll, D., 2022. Forest expansion dominates China's land carbon sink since 1980. Nat. Commun. 13, 5374.

Yuan, H., Dai, Y., Xiao, Z., Ji, D., Shangguan, W., 2011. Reprocessing the MODIS leaf area index products for land surface and climate modelling. Remote Sens. Environ. 115 (5), 1171–1187.

Zeng, Y., Hao, D., Park, T., Zhu, P., Huete, A., Myneni, R., Knyazikhin, Y., Qi, J., Nemani, R.R., Li, F., 2023. Structural complexity biases vegetation greenness measures. Nat. Ecol. & Evolut. 1–9.

Zhang, A., Jia, G., Epstein, H.E., Xia, J., 2017a. ENSO elicits opposing responses of semi-arid vegetation between hemispheres. Sci. Rep. 7, 42281.

Zhang, Y., Song, C., Band, L.E., Sun, G., Li, J., 2017b. Reanalysis of global terrestrial vegetation trends from MODIS products: Browning or greening? Remote Sens. Environ. 191, 145–155. https://doi.org/10.1016/j.rse.2016.12.018.

Zhang, Y., Dannenberg, M.P., Hwang, T., Song, C., 2019a. El Niño-southern oscillation-induced variability of terrestrial gross primary production during the satellite era. J. Geophys. Res. Biogeosci. 124, 2419–2431.

Zhang, Y., Song, C., Band, L.E., Sun, G., 2019b. No proportional increase of terrestrial gross carbon sequestration from the greening earth. J. Geophys. Res. Biogeosci. 124, 2540–2553.

Zhang, Y., Song, C., Hwang, T., Novick, K., Coulston, J.W., Vose, J., Dannenberg, M.P., Hakkenberg, C.R., Mao, J., Woodcock, C.E., 2021. Land cover change-induced decline in terrestrial gross primary production over the conterminous United States from 2001 to 2016. Agric. For. Meteorol. 308–309, 108609. https://doi.org/10.1016/j.agrformet.2021.108609.

Zhang, Y., Mao, J., Ricciuto, D.M., Jin, M., Yu, Y., Shi, X., Wullschleger, S., Tang, R., Liu, J., 2023. Global fire modelling and control attributions based on the ensemble machine learning and satellite observations. Sci. Remote Sens. 7, 100088.

Zhao, Q., Zhu, Z., Zeng, H., Zhao, W., Myneni, R.B., 2020. Future greening of the earth may not be as large as previously predicted. Agric. For. Meteorol. 292–293, 108111. https://doi.org/10.1016/j.agrformet.2020.108111.

Zhou, S., Liang, J., Lu, X., Li, Q., Jiang, L., Zhang, Y., Schwalm, C.R., Fisher, J.B., Tjiputra, J., Sitch, S., Ahlström, A., Huntzinger, D.N., Huang, Y., Wang, G., Luo, Y., 2018. Sources of uncertainty in modeled land carbon storage within and across three MIPs: diagnosis with three new techniques. J. Clim. 31, 2833–2851. https://doi.org/10.1175/JCLI-D-17-0357.1.

Zhu, Z., Piao, S., Myneni, R.B., Huang, M., Zeng, Z., Canadell, J.G., Ciais, P., Sitch, S., Friedlingstein, P., Arneth, A., Cao, C., Cheng, L., Kato, E., Koven, C., Li, Y., Lian, X., Liu, Y., Liu, R., Mao, J., Pan, Y., Peng, S., Peñuelas, J., Poulter, B., Pugh, T.A.M., Stocker, B.D., Viovy, N., Wang, X., Wang, Y., Xiao, Z., Yang, H., Zaehle, S., Zeng, N., 2016. Greening of the earth and its drivers. Nat. Clim. Chang. 6, 791–795. https://doi.org/10.1038/nclimate3004.